

This report is based on studies performed at Lincoln Laboratory, a center for research operated by Massachusetts Institute of Technology. The work was sponsored by the U.S. Army Strategic Defense Command, Department of the Army under Air Force Contract F19628-90-C-0002.

This technical report has been reviewed and is approved for publication.

FOR THE COMMANDER

Hugh L. Southall

Hugh L. Southall, Lt. Col., USAF
Chief, ESD Lincoln Laboratory Project Office

Non-Lincoln Recipients

PLEASE DO NOT RETURN

Permission is given to destroy this document
when it is no longer needed.

MASSACHUSETTS INSTITUTE OF TECHNOLOGY
LINCOLN LABORATORY

BIOCHIP TECHNOLOGY DEVELOPMENT

H.E. ZEULI

Group 61

D.K. ASTOLFI

S.G. CANN

D.J. EHRLICH

Group 81

D.L. HOVEY

Group 85

Y.V. GRINBUSH

Group 87

M.D. EGGERS

T.S. KHUON

R.Y. LEVINE

Group 93

TECHNICAL REPORT 901

9 NOVEMBER 1990

Approved for public release; distribution is unlimited.

LEXINGTON

MASSACHUSETTS

ACKNOWLEDGMENTS

We owe great debt to the many people who generously contributed to the pioneering spirit and enthusiasm that drove this project along many challenging avenues. We specifically acknowledge the generous counseling provided by Bob Rafuse and the constructive criticism offered by Professor Jerry Lettvin. Also we wish to thank both the Lincoln Laboratory Publications Group and Library for their efficient and excellent services.

Finally, we sincerely thank Walter Morrow and those individuals instrumental in establishing the Innovative Research Program at Lincoln Laboratory, which financially supported the work. The opportunity proved incredibly stimulating to all involved.

TABLE OF CONTENTS

| | |
|--|-----|
| Abstract | iii |
| Acknowledgments | v |
| List of Illustrations | ix |
| List of Tables | xi |
| 1. INTRODUCTION | 1 |
| 2. BIOCHIP ENGINEERING | 5 |
| 2.1 Biophysical Signal Source | 5 |
| 2.2 Microcircuit Electrode Design | 12 |
| 2.3 Microcircuit Electrode Array Fabrication | 31 |
| 2.4 Microcircuit Electrode Array Evaluation | 36 |
| 2.5 System Integration | 38 |
| 3. NEURAL GROWTH BIOLOGY | 45 |
| 3.1 Dissociated Cell Cultures | 45 |
| 3.2 Clonal Cell Cultures | 45 |
| 4. NEURAL MEASUREMENTS | 47 |
| 4.1 Neuron Recording | 47 |
| 4.2 Neuron Stimulation | 48 |
| 5. CONCLUSION | 53 |
| 6. REFERENCES | 55 |

LIST OF ILLUSTRATIONS

| Figure No. | | Page |
|---------------|---|------|
| 1 | Illustration of the biochip concept. | 3 |
| 2 | Electrical signals processed by neurons. | 5 |
| 3 | Intracellular and extracellular recording methods. | 6 |
| 4 | Electrical circuit analogy representing the passive neural membrane properties. | 9 |
| 5 | Membrane rest and action potentials. | 10 |
| 6 | (a) Diagram of microcircuit electrode exposed to a homogeneous conducting solution for extracellular recording with accompanying (b) electrical equivalent circuit, and (c) reduced equivalent circuit. | 13 |
| 7 | Permissible current paths from electrode to ground ring. | 14 |
| 8 | Formation of the electrical double layer from (a) initial reaction to (b) final equilibrium. | 15 |
| 9 | Voltage profiles of (a) Helmholtz and (b) Gouy-Chapman electric double-layer models. | 16 |
| 10 | Diagram of (a) calibration experiment and (b) equivalent circuit. | 18 |
| 11 | Experimental calibration constants. | 19 |
| 12 | Electrode line with conducting and adhesion layers. | 20 |
| 13 | Cross-section of shunt capacitance between the electrode and electrolyte. | 20 |
| 14 | Dimension labeling of microcircuit electrode. | 21 |
| 15 | Impedance reduction of equivalent circuit. | 23 |
| 16 | Diagram of (a) simple and (b) circular bipolar electrodes. | 29 |
| 17 | Biochip fabrication procedure. | 32 |
| 18 | Electrode (a) impedance and (b) colloidal surface layer following platinization. | 33 |
| 19 | Unipolar (a) biochip with (b) 72-electrode array. | 34 |
| 20 | Bipolar (a) biochip with (b) 34-electrode array. | 35 |
| 21 | Theoretical and measured biochip electrode impedances. | 37 |
| 22 | Theoretical and measured platinized biochip electrode impedances. | 38 |

LIST OF ILLUSTRATIONS (Continued)

| Figure No. | | Page |
|---------------|---|------|
| 23 | Neural network signal processing system. | 39 |
| 24 | Data acquisition host computer system. | 40 |
| 25 | Data acquisition modules for interfacing with the biochip and host computer. | 40 |
| 26 | Schematic of (a) instrumentation amplifier and (b) corresponding frequency response. | 42 |
| 27 | Warm-blooded neuronal chamber. | 43 |
| 28 | Cold-blooded neuronal chamber | 44 |
| 29 | Clonal cell generation. | 46 |
| 30 | Single-neuron recording from conventional and biochip electrodes. | 48 |
| 31 | Electron micrograph of synaptically connected neurons on biochip surface. | 49 |
| 32 | Recorded signals from artificially stimulated, synaptically coupled neurons on biochip surface. | 50 |
| 33 | Recorded signals from spontaneously active, synaptically coupled neurons on biochip surface. | 50 |
| 34 | On-chip neuron stimulation results using unipolar biochip electrode. | 51 |

LIST OF TABLES

| Table No. | | Page |
|----------------------|---|-------------|
| 1 | Microcircuit Electrode Equivalent Circuit | 21 |
| 2 | Dimensions for Plausible Electrode Designs | 22 |
| 3 | Simple and Circular Bipolar Design Dimensions | 30 |
| 4 | Theoretical and Measured Biochip Electrode Impedances | 37 |

1. INTRODUCTION

Today the study of biological intelligence constitutes perhaps the most challenging yet rewarding frontier of research. A most compelling notion attracting many researchers is that such complex intelligence originates from a vast interconnected architecture containing approximately 10^{12} relatively simple computational units or neurons. This massively parallel architecture, sporting approximately 10^{15} adaptable neural interconnectors, is responsible for the extraordinary pattern processing capabilities of the brain.

Among the pattern processing capabilities of interest to machine intelligence researchers pursuing engineering applications are fast pattern recognition by association, apparent infinite memory capacity, generalization, and robust, fault-tolerant performance. Furthermore, these system level capabilities are obtained biologically at modest expense, for the human brain consumes energy at a rate comparable to that of a single VLSI digital signal processing chip. Such efficiency arises from the rather conservative processing units, operating with 1 ms time constants and slowly communicating information (100 ms) along passive neuronal channels. Although the components are relatively sluggish (in comparison to conventional digital computers containing nanosecond processors performing millions of instructions per second) the nervous system is capable of quickly (10 ms) recognizing patterns in environments that continue to elude conventional computing. That is, biologically, a fast, reliable system emerges from numerous slow, noisy components.

In conjunction, the recent neural network computing approaches to pattern processing, such as those proposed by Hopfield [1], Grossberg [2], Kohonen [3], Rumelhart and McClelland [4], capture certain biological network properties including recognition by association, distributed parallel processing, and generalization. For example, Sejnowski [5] in months' time demonstrated the associative memory capability of the multilayer perceptron by configuring a neural network to learn the phoneme transcription rules necessary to produce synthesized speech from text. A similar task accomplished by classical techniques employing specific parametric models and explicit expert rules required years. Other examples include computer simulations by Linsker [6], which suggest that neural networks with pattern-processing properties as complex as those found in the mammalian visual system can evolve from simple adaptations in the neural interconnections during development. Such results imply that the nature of biological pattern-processing systems can be understood (and imitated) if the rules governing neural architecture development are known. From work conducted at Lincoln Laboratory [7-9] and elsewhere, many mathematical neural network models often perform similarly to classical approaches on established problems yet do not require *a priori* parametric models, statistics, or expert rules. These mathematical networks, adapted to given tasks through learning processes driven by available training data, seem to substantiate the ever-prevailing wisdom acknowledging the suitability of neural-like architectures for pattern recognition and other random problems where algorithmic solutions do not exist [10].

Although recent neural-network models offer an inspiring beginning, a vast performance gap remains between these silicon implementations and their biological counterparts. Because this vast difference is due to our limited knowledge of the system properties arising from neuronal architectures, the development of a biological/electronic technology is warranted and aimed at providing system-level tools for exploring, modeling, and exploiting biological pattern-processing capability.

1.1 BACKGROUND

Basically, brain architecture development is a two-stage process. First, during neurogenesis, cells are rapidly generated, differentiate into specific neural types, and are properly positioned within the developing brain. This first stage builds and positions all the processing units (neurons) within the architecture. Following neurogenesis, lifelong synaptogenesis refines the architecture by adapting the interconnections among the processors. The adaptation of the synaptic interconnections depends on electrical signaling from neighboring neurons. The importance of such network sensory stimuli in shaping the synaptic architecture of the nervous system is made clear by studies on both the visual and motor systems. In fact, many neurobiologists believe the higher brain functions, including disposition, learning, and memory, reside in the actual geometry and adaptation capability of these neural synapses [11].

Because the experimental techniques needed to monitor and regulate electrical activity during neural synapse development are not available, the role played by electrical information in establishing synaptic architecture at the cellular and molecular levels remains a mystery. Specifically, conventional single cell intracellular recording and stimulation techniques are inadequate to characterize synaptic network phenomenon due to limitations in quantity and time. That is, micromanipulation requirements needed to bring conventional electrodes to the cells limit the number of electrodes (approximately three) placed into a restricted brain area containing thousands of neurons, thereby sampling only a fraction of the neurons involved in a given network. More recently, optical imaging methods have been developed that have the potential to monitor multiple cells simultaneously in culture. However, these techniques cannot be used for stimulation — a crucial feature for detailed synaptogenesis study. In addition, many molecular changes take place over long periods, often several days to weeks. With micromanipulation, keeping electrodes in good contact for more than a few hours is difficult. Finally, intracellular recording can be a rather exhausting experience for both the experimenter and host neuron, since the 0.1- μm diameter glass micropipette electrode must be inserted just inside the 0.01- μm thick cellular membrane when experimenting with a typical mammalian (10- μm) neuron. Consequently, conventional cell-recording techniques may be suited to the study and classification of single neurons but are inadequate for providing system-level information necessary to describe the collective behavior of many neurons composing the network.

To extract a more complete picture of network behavior, various multielectrode microcircuits have been developed for *in vitro* experimentation. Thomas *et al.* [12] are credited for the novel concept of bringing cells to the sensor rather than bringing the sensor to the cells. Sheets of heart cells were grown on the surface of microcircuit substrates embedded with 30 electrodes. Although network behavior was observed from the spontaneous rhythmic contractions, no electrical recordings from single cells were obtained. Later, Gross [13, 14] and Pine [15] successfully obtained electrical recordings from neurons clustered on substrates. A critical factor determining the success of electrical recording was the impedance of the electrode. With low electrode impedances ($<1\text{M}\Omega$), satisfactory recordings resulted with good signal-to-noise ratios (SNR). To reduce electrode impedance, Gross [13] developed a laser deinsulating technique that increased the effective area of the electrode, while Pine [15] plated the electrodes with platinum black to achieve similar results.

These multielectrode microcircuit contributions have demonstrated basic network phenomenon *in vitro*, including rhythmic activity and patterned bursting, although such properties were already known from single-cell recording. However, quantitative network analysis necessary to support an understanding of biological pattern processing remains plagued by the extraordinary number of degrees of freedom that arise from cultures (of multiple neuronal types) that greatly exceed the size of the recording matrix. It is, therefore, important to reduce the complexity by monitoring smaller networks more completely.

1.2 BIOCHIP CONCEPT

Inspired by the earlier microcircuit works cited, the report describes the development of a biological compatible microcircuit technology aimed at interfacing living neural networks and computers for network experimentation. The concept of the "biochip" is illustrated in Figure 1. Basically, an array of microelectrodes embedded in a biologically compatible substrate is fabricated using conventional micro-fabrication techniques. Because the electrodes are embedded in the surface, neurons can grow in contact with the electrodes and their electrical properties can be monitored as the neurons differentiate. The approach presented differs from those cited in that neural network complexity is reduced by selectively choosing and placing neurons on the microcircuit, preferably one or more electrodes per neuron. Specifically, identified, individually harvested *Aplysia* neurons with known transmitters are placed over the electrodes that generate synaptic connections with neighboring neurons. Also, identical (cloned) immortalized precursors of neurons are also placed on the biochip to obtain a stereotyped network, greatly reducing mathematical complexity. The potential exists for placing identical class neurons in columns on the microcircuit, where each column would represent a specific neural layer found in a portion of the brain of interest.

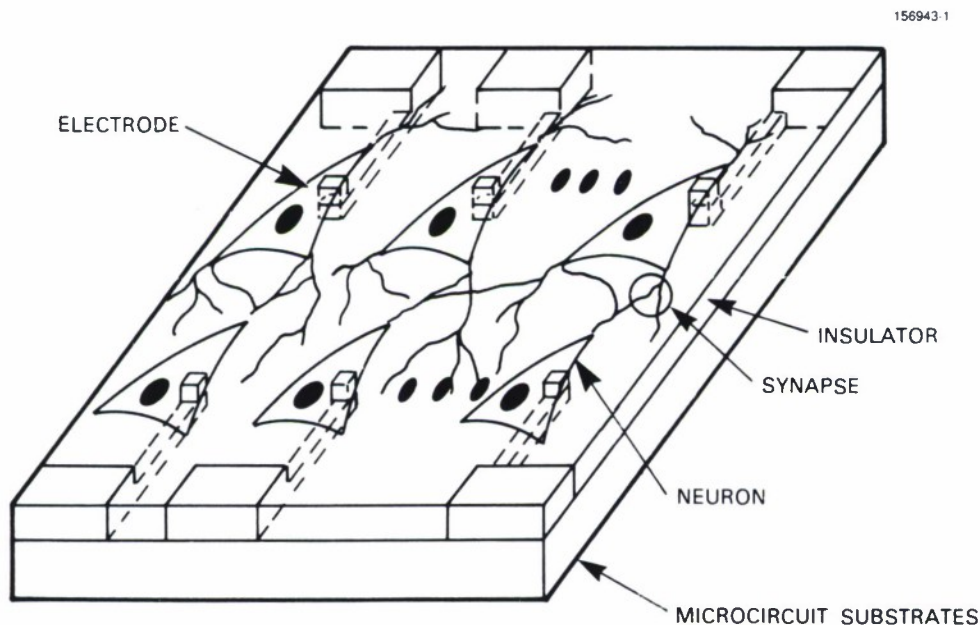


Figure 1. Illustration of the biochip concept.

The development of a novel biochip stimulation capability is presented to improve the analysis of the mechanisms by which electrical stimulation influences synaptic architecture modification. Here both global and local (single neuron) on-chip stimulation techniques are described using customized electrodes. Finally, a significant contribution lies in the theoretical electrode modeling, design, and evaluation procedures presented with supporting calibration experiments.

Overall, the biochip technology presented describes the engineering, biology, and resulting measurements obtained from the microelectrode arrays suitable for electronically interfacing living neuronal networks. First, electrical engineering efforts are discussed, including the characterization of the biophysical neural signals together with the design, fabrication, evaluation, and system integration. Next, biological aspects are presented that describe both dissociated and clonal neural cell growth methods established using the biochip. Finally, the integration of both engineering and biology is reflected by the final neural measurements section that demonstrates both on-chip, noninvasive recording and stimulation capability.

2. BIOCHIP ENGINEERING

2.1 BIOPHYSICAL SIGNAL SOURCE

The neuron is an information processor that relies on electrical signaling for both short- and long-distance communication. Signal processing tasks performed efficiently by a neuron include the routine integration of approximately 1,000 input signals. The low frequency (<100 Hz)/low-voltage (0.1-10 mV) transduced neural inputs arise from neighboring synaptically coupled neurons. Often referred to as postsynaptic potentials, these local transmission signals are either inhibitory or excitatory, as displayed in Figure 2. A postsynaptic signal generated by an excitatory synapse contributes to neural firing (emission of long-distance communication) while, conversely, an inhibitory synaptic connection suppresses the activity.

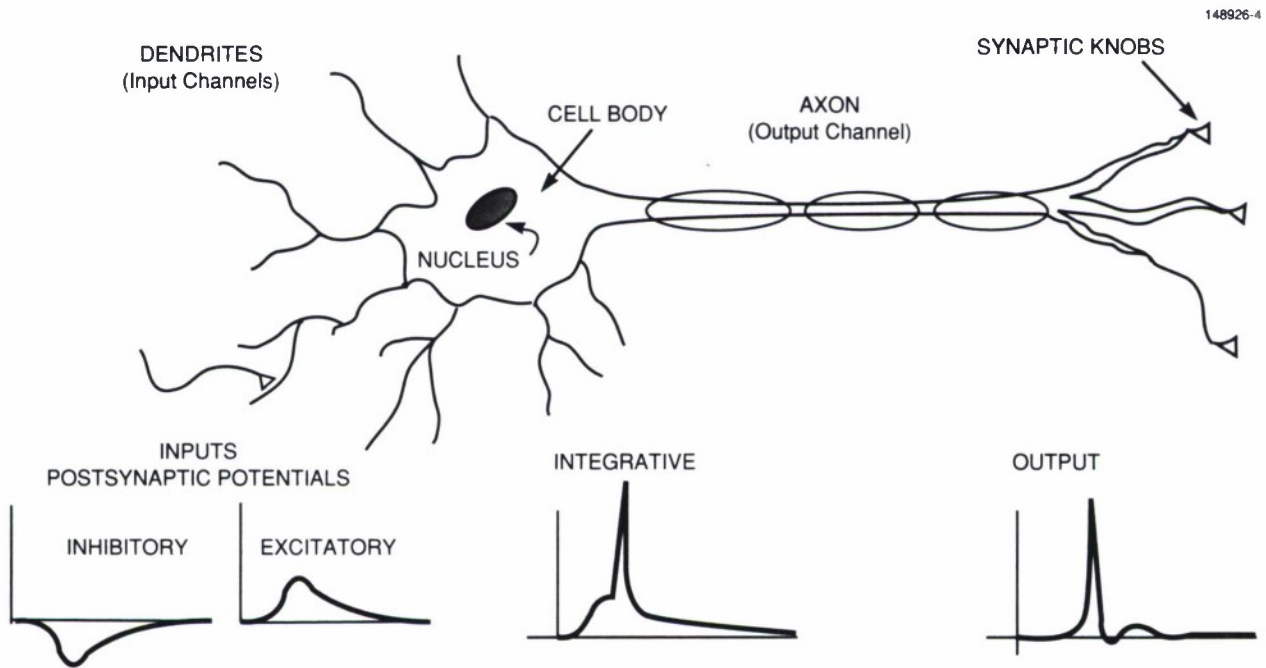


Figure 2. Electrical signals processed by neurons.

Following signal integration, the neuron provides long-distance communication by transmitting high-frequency (1 kHz)/high-voltage (70-110 mV) pulses along the output channel (axon) as shown in Figure 2. Because the initial intent is to investigate the collective properties of a neural network, these high-frequency, long-distance signals that subserve network communication are of primary interest.

Neural signal recording pertains here to recording the long-distance transmissions that originate at the cell body and propagate down the axon.

The signal recording can be achieved via intracellular (conventional) or extracellular techniques. The signal obtained during intracellular recording is described first, leading to an understanding of the physical processes governing the signal generation. Next, the related extracellular signal obtained when recording from the biochip electrodes is described.

2.1.1 Intracellular Signal

The intracellular signal previously discussed is known as the membrane potential, because the voltage signal is due to the electrical charge imbalance across the biological membrane. Basically the bulk solution inside (cytoplasm) and outside (extracellular fluid) the membrane is electrically neutral as diagrammed in Figure 3. However, ions are unequally distributed within approximately $1\ \mu\text{m}$ of the intracellular and extracellular membrane surfaces, giving rise to the localized membrane potential. At rest, the extracellular surface is more positive than the intracellular surface, resulting in a negative membrane potential when recording with a conventional glass-coated intracellular microelectrode.

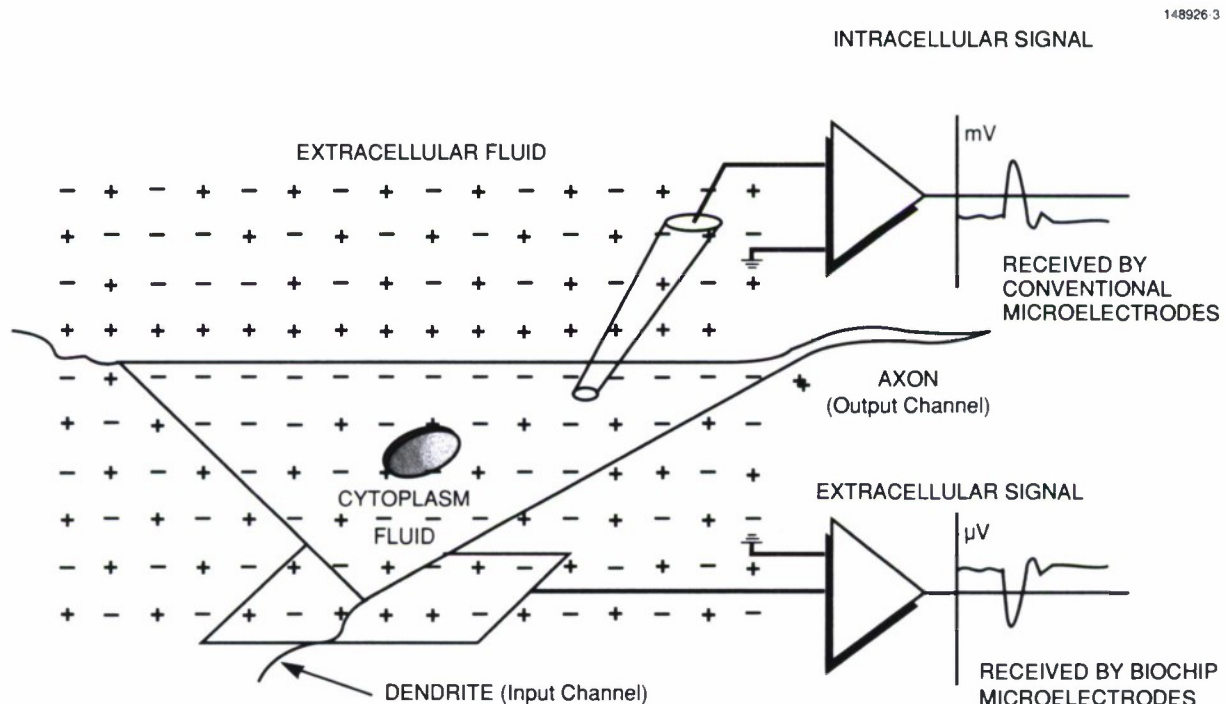


Figure 3. Intracellular and extracellular recording methods.

Three ions are involved in establishing this membrane potential, sodium (Na^+), potassium (K^+), and chloride (Cl^-). The generation of the large membrane potentials for long-distance transmission is due to a change in membrane permeability that effectively alters the distribution of these ions across the membrane. Because the ions are driven by physical forces, specifically electrical and chemical concentration energy gradients, the membrane potential can be quantitatively expressed in terms of the individual ionic permeabilities and concentrations at the neural membrane.

First, the general steady-state equation describing the current produced by a single ion under the influence of both the chemical concentration and electrical gradients is formulated in terms of the membrane potential (Nernst-Planck equation). Next, the equation is solved under the constant-electric-field assumption (Goldman equation). When all three ions are included, the resulting expression at equilibrium yields the membrane potential as a function of the specific membrane permeabilities and ionic concentrations (Goldman-Hodgkin-Katz equation). Finally, an alternative simple expression for the membrane potential, derived from an electrical-circuit analogy, is presented (Hodgkin-Huxley equation).

The basic principle governing ionic signaling is that an energy gradient produced by a variation in temperature, pressure, chemical concentration, voltage, or any combination thereof, across a membrane produces a force that drives the ion through a permeable membrane; thus an electrical current ($i = dq/dt$), or equivalently a flux ($J = i/\text{area}$) is generated. Simply, the flux is directly proportional to the force,

$$J = \alpha F \quad (1)$$

where

$$F = \sum_i \frac{dG_i}{dx} \quad (2)$$

and the net force is an accumulation of the Gibbs free-energy gradients. Considering only a variation in ionic concentration and voltage across a membrane, the flux reduces to (Nernst-Planck)

$$J = -D \frac{dc}{dx} - K \frac{dV}{dx} \quad (3)$$

where $D = uRT = pL$ is the diffusion coefficient, $K = uc_zF$ is the electrical conductivity, u is the ion mobility $[(\text{m/sec})/(\text{joule/m})]$, c is the concentration (moles/m^3), p is the permeability of the membrane of thickness L to a given ion, z is the ionic valence, and F is the Farraday constant (96,500 coul/mole). The flux is seen to be a linear function of the concentration and electrical gradients. Also from (3), the voltage across the membrane at equilibrium, defined where the concentration gradient is equal and opposite to the electrical gradient, can be easily determined by zeroing the flux (Nernst)

$$\begin{aligned} dV &= \frac{-D}{K} dc \quad (J = 0) \\ \Rightarrow V' &= \frac{-RT}{zF} \ln \frac{c^i}{c^o} \end{aligned} \quad (4)$$

where c^i and c^o are the ionic concentrations just inside and outside the membrane, respectively. Such

single-ion equilibrium voltage can be calculated for each ion knowing the relative concentrations across the membrane; this is known as the Nernst potential.

Assuming a constant electric field $\left(\frac{dV}{dx} = E\right)$, the Nernst-Planck equation (3) can be solved to yield

$$J = \frac{-p(zF)^2}{RT} V \left[\frac{c^o - c^i e^{zFV/RT}}{1 - e^{zFV/RT}} \right] \quad (5)$$

Furthermore, the steady-state flux equation for the complete neural membrane system can now be obtained by expressing the total flux in terms of the independent contributions from each of the three ionic species accordingly (Goldman-Hodgkin-Katz)

$$\begin{aligned} J &= J_K + J_{Cl} + J_{Na} \\ &= \frac{-F^2 V}{RT(1 - e^{FV/RT})} \left\{ (p_K c_K^o + p_{Na} c_{Na}^o + p_{Cl} c_{Cl}^i) \right. \\ &\quad \left. - e^{FV/RT} (p_K c_K^i + p_{Na} c_{Na}^i + p_{Cl} c_{Cl}^o) \right\} \quad (6) \end{aligned}$$

As with the single-ion system, the voltage across the membrane at equilibrium for the more realistic multiple-ion system is determined by setting $J = 0$ in (6) and solving for the resulting equilibrium voltage (Goldman-Hodgkin-Katz)

$$V' = \frac{RT}{F} \ln \left(\frac{p_K c_K^o + p_{Na} c_{Na}^o + p_{Cl} c_{Cl}^i}{p_K c_K^i + p_{Na} c_{Na}^i + p_{Cl} c_{Cl}^o} \right) \quad (7)$$

The net current (6) through and voltage (7) across the neural membrane are a function of the individual ionic membrane permeabilities and ionic concentrations.

The voltage/current characteristics of the neural membrane can be alternatively expressed by an electrical circuit analog. Regarding the passive properties of the neural membrane as a resistor with individual conductance values for each ion, the ionic currents can be expressed (Hodgkin-Huxley)

$$i_{Na} = g_{Na} (V - V_{Na}) \quad (8)$$

$$i_K = g_K (V - V_K) \quad (9)$$

$$i_{Cl} = g_{Cl} (V - V_{Cl}) \quad (10)$$

The bias voltages V_{Na} , V_K , and V_{Cl} are the single-ion equilibrium voltages given by the Nernst potential (4). These voltages are included to ensure that no particular ion flow occurs when the membrane potential

reaches an ion's equilibrium voltage (for example $i_{Na} = 0$ when $V = V_{Na}$). Overall, the membrane system is in equilibrium when the net current across the membrane reaches zero ($i = i_{Na} + i_K + i_{Cl} = 0$), yielding the system equilibrium voltage

$$0 = g_{Na}(V' - V_{Na}) + g_K(V' - V_K) + g_{Cl}(V' - V_{Cl})$$

$$\therefore V' = \frac{g_K V_K + g_{Na} V_{Na} + g_{Cl} V_{Cl}}{g_K + g_{Na} + g_{Cl}} \quad (11)$$

In comparison with (7), by using empirically derived membrane conductances instead of membrane permeabilities and ionic concentrations, a much simpler formulation of (11) results with much intuitive appeal. Moreover, the membrane can now be easily represented by an equivalent circuit, given the v/i relationships (8-10) as shown in Figure 4. The model incorporates variable conductances for both K and Na; the variation in these conductances accounts for the two basic states of the membrane potential.

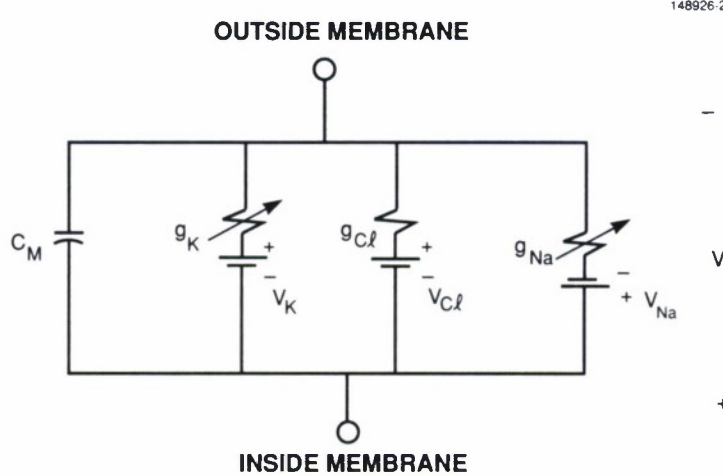


Figure 4. Electrical circuit analogy representing the passive neural membrane properties.

The two membrane potential states, resting and action, are depicted in Figure 5. The intracellular resting potential is typically around -40 mV to -75 mV. The action potential suitable for long-distance communication is a short-duration pulse (about 1 ms) with large magnitude (typically 40 - 70 mV). The origin of these potentials can be described in terms of the previously outlined membrane equations.

To gain intuition, the formulation first presents the resting potential for an ideal neuron. At rest, the ideal neuron is totally impermeable to Na^+ ; therefore, $i_{Na} = 0$ even though both the concentration and electrical gradients for Na^+ are forcing the ion into the cell. Also, the concentration of K^+ is approximately

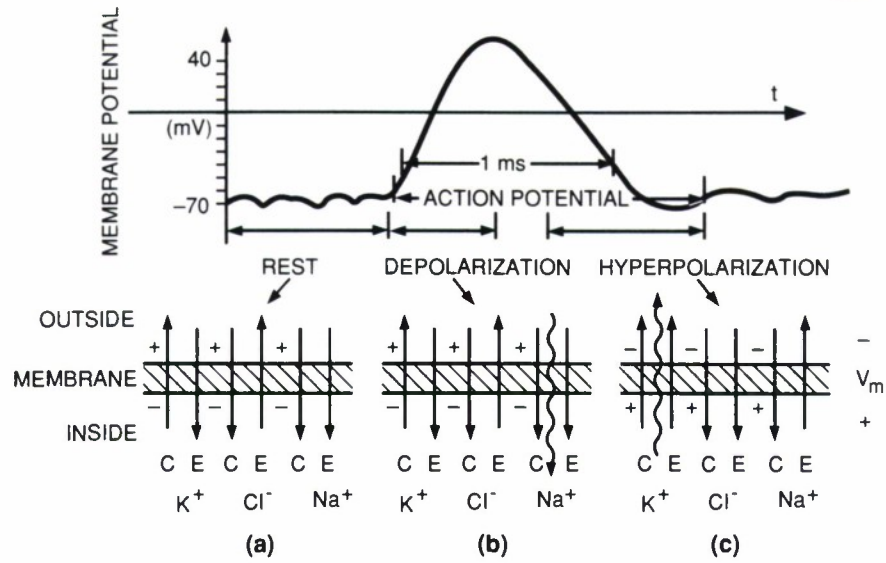


Figure 5. Membrane rest and action potentials.

thirty times greater inside the cell, while the concentration of Cl^- is approximately thirty times greater outside the cell. As a consequence, the ionic equilibrium (Nernst) potentials become

$$V_K = \frac{-RT}{F} \ln\left(\frac{30}{1}\right) \cong -85\text{mV} \quad (12)$$

$$V_{\text{Cl}} = \frac{RT}{F} \ln\left(\frac{1}{30}\right) \cong -85\text{mV} \quad (13)$$

The electrical and chemical gradients are then equal and opposite for both K^+ and Cl^- at a membrane potential of -85 mV , thus preventing ion flow. Specifically, the diffusion force driving K^+ outside the membrane (because of the greater inside concentration) is countered by the electric-field force established at -85 mV that drives the positive-charged ion back across to the inside of the membrane. In theory, the membrane can sustain this ideal neuron resting state forever.

In reality, the neuronal membrane is slightly impermeable to Na^+ at rest, and the concentration ratios for Cl^- and K^+ are unequal. Therefore, the system equilibrium voltage ($\approx -70\text{mV}$) is established by all three ions according to (7), where K^+ plays a dominant role because of the large K^+ permeability. For the realistic case the net current ($i = i_{\text{Na}} + i_{\text{Cl}} + i_{\text{K}}$) is again zero at equilibrium, but the individual passive currents are not zero (as they were in the ideal case). The movement of Na^+ into the cell is balanced by the outward movement of K^+ . However, these passive counter fluxes can not continue indefinitely; in time the interior K^+ would be depleted and Na^+ would increase, altering the controlling gradients. The gradients are maintained by a $\text{Na} - \text{K}$ pump that pumps Na^+ out and K^+ in. Thus, in the realistic neuronal membrane at rest, metabolic energy must be supplied to maintained the ionic gradients.

As displayed in Figure 5(b) and 5(c), the action potential represents the active signaling state of the membrane potential and is divided into regions of depolarization and hyperpolarization. These states result from radical changes in the membrane permeability caused by the opening and closing of voltage-controlled gated channels in the membrane.

In depolarization, the gated Na^+ channels are opened when the membrane potential is raised approximately 15 mV beyond the resting potential created by the integrated excitatory response of neighboring synaptically connected neurons. The exact mechanisms supporting the opening of these voltage-controlled membrane channels are unknown. The net effect is that the membrane permeability to Na^+ increases by a factor of near 500; driven by the favorable concentration gradient, Na^+ rushes through the membrane into the cell. The interior of the cell membrane becomes appreciably more positive which, in turn, drastically increases the intracellular membrane potential. Quantitatively, the membrane potential climbs according to (7), where now Na^+ with a very large permeability (P_{Na}) dominates the expression, resulting in a potential ($\sim 40\text{mV}$) near the Nernst potential for Na^+ ($\sim 55\text{mV}$). Depolarization can be alternatively viewed as a radical change in the membrane conductance to Na^+ , which in turn causes a voltage increase according to (11) from the electrical circuit analogy.

Hyperpolarization is due to a radical change in the membrane permeability to K^+ prompted by the opening of voltage-controlled K^+ gated membrane channels. These channels, like the Na^+ channels, are opened when the membrane potential rises from its resting level. The difference is that the gating of K^+ channels happens with a delay, permitting the large influx of Na^+ ions before K^+ channels open to allow the efflux of K^+ . The delayed flow of K^+ ions through the gated channels into the extracellular fluid tends to counter the flow of Na^+ ions into the cell, forcing the membrane voltage back to the resting potential where the voltage-controlled channels are once again closed. Hyperpolarization can be alternatively viewed in terms of changing conductances in the equivalent electrical circuit, Figure 4, where now g_{K} varies substantially.

2.1.2 Extracellular Signal

The extracellular signal arises from the electrical charge imbalance near the outside of the biological membrane. In contrast to the intracellular potential, this potential is recorded outside the neural membrane and with respect to the neutral extracellular fluid as diagrammed in Figure 3. The ionic basis for extracellular signaling is the same as discussed in the previous section; however, in this case the signal polarity is reversed and the magnitude is substantially reduced, because the difference in ionic concentrations near the extracellular membrane surface and the extracellular fluid is much less. The extracellular potential is typically in the microvolt range, while the intracellular potential is measured in millivolts. The three order-of-magnitude decrease in signal strength warrants careful electrode modeling and design.

In conclusion, the biophysical signal source for neural-network communication arises from a variation in the ionic concentrations near the neural membrane. This variation in ion concentration is due to drastic changes in membrane permeability to selected ions, produced by the gating of ion-selective voltage-controlled membrane channels. Although the surrounding synaptically connected neurons are responsible for generating these gating voltages, the exact molecular basis for the process is currently unknown.

2.2 MICROCIRCUIT ELECTRODE DESIGN

The design objective is to specify the dimensions of an optimal microcircuit electrode for both extracellular recording and stimulation of interconnected neurons. The procedure entails specifying an objective (cost) function necessary to mathematically define the optimal performance. Optimizing this function yields a set of dimensions for the optimal electrode design. Consequently, the design approach involves first expressing the electrical characteristics of the electrode in terms of the microcircuit dimensions, then defining a cost function in terms of these electrical characteristics, and, finally, optimizing the cost function to yield the optimal electrode design.

2.2.1 Equivalent Circuit Components

The electrical characteristics of a microelectrode in a homogeneous conducting medium can be modeled as an equivalent circuit, with each electrical component expressed in terms of the fundamental electrode dimensions (see Figure 6). These components are described and derived in the following paragraphs. The general approach follows the treatment of Robinson [16] for conventional glass-coated wire electrodes; however, new techniques are presented where appropriate for the specific microfabrication application.

V_s — *Voltage Source*

In order to derive a simple electrode circuit, the neuron is modeled as an ideal voltage source. The voltage V_s is equal to the extracellular voltage that would be recorded immediately outside the axon wall, and is referenced to the electrically neutral homogeneous conducting solution. The voltage source is in series with the spreading resistance R_s , so that removal of the neuron ($V_s = 0$) results in the proper circuit depicting the current flow in a homogeneous conducting solution.

R_s — *Spreading Resistance*

The spreading resistance R_s is the resistance of the homogeneous conducting solution between the metallic electrode and the metal ground ring (designated infinity). The resistance can be derived by integrating the differential resistance along the current path according to

$$R_s = \int_{r_o}^{r_{oo}} dR \quad . \quad (14)$$

An expression is readily obtained, providing the current path is perpendicular to the conducting surfaces. In such case, the differential resistance is

$$dR = \rho \frac{dr}{A(r)} \quad (15)$$

where ρ is the resistivity ($\Omega \cdot m$), dr is the differential current path, and $A(r)$ is the conducting surface area. By slightly distorting the shape of both the electrode and ground ring (while maintaining original surface area) as shown in Figure 7, the current flow is constrained to perpendicular, resulting in the expression

$$R_s = \rho \int_{r_0}^{\infty} dr / 2\pi r^2 \cos \phi_0 \quad . \quad (16)$$

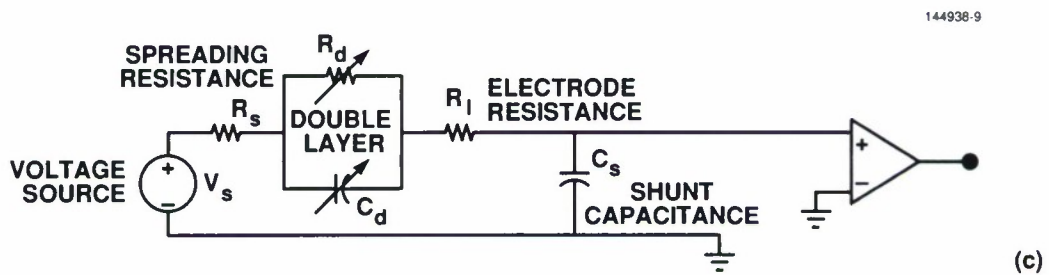
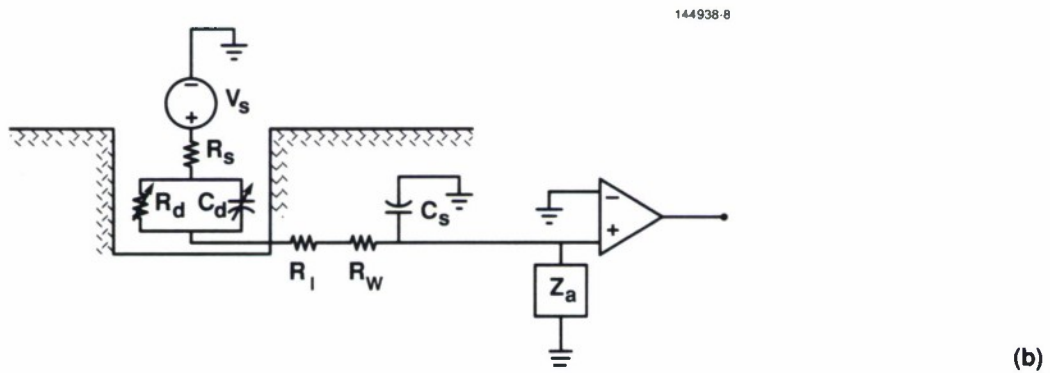
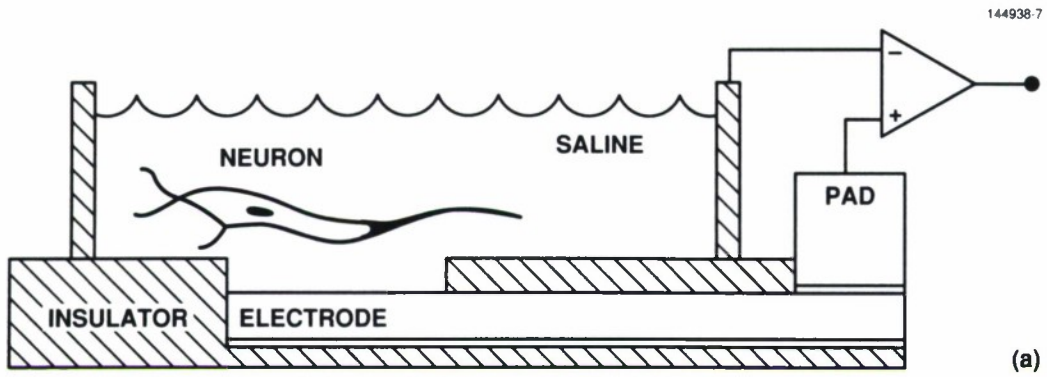


Figure 6. (a) Diagram of microcircuit electrode exposed to a homogeneous conducting solution for extracellular recording with accompanying (b) electrical equivalent circuit, and (c) reduced equivalent circuit.

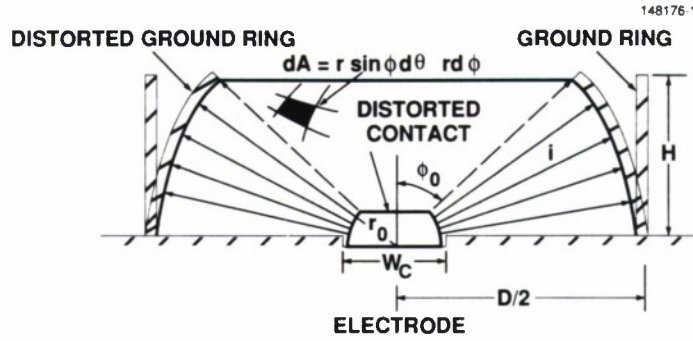


Figure 7. Permissible current paths from electrode to ground ring.

Moreover, r_0 and ϕ_0 are calculated by equating the surface areas of the distorted and actual conductive surfaces. For the square electrode surface

$$\begin{aligned} W_c^2 &= 2\pi r_0^2 \cos \phi_0 \\ \therefore r_0 &= W_c / \sqrt{2\pi \cos \phi_0} \end{aligned} \quad (17)$$

and for the ground-ring cylindrical surface

$$\begin{aligned} 2\pi \left(\frac{D}{2}\right) H &= 2\pi \left(\frac{D}{2}\right)^2 \cos \phi_0 \\ \therefore \cos \phi_0 &= 2H / D \end{aligned} \quad (18)$$

Substituting (17) and (18) into (16) yields the spreading resistance

$$R_s = \frac{\rho}{W_c \sqrt{4\pi H / D}} \quad (r_\infty \gg r_0) \quad (19)$$

where H and D are the height and diameter of the ground ring, and W_c is the width of the square electrode contact.

R_d, C_d —Double Layer Resistance and Capacitance

The complex electrochemical reactions at the interface of the metal electrode and electrolyte constitute an electric double layer, which is the most challenging phenomenon to model. The electric double layer arises from the potential difference that naturally exists at every metal-solution interface. The magnitude of the potential depends on the electronic work function of the metal, the energy of adsorption on the metal from components of the reaction, energy of chemical bonds between the metal and reactants, and the hydration energy. The net sum of these energies produces a chemical gradient that forces the charge transfer reaction in one direction as illustrated in Figure 8(a). As the reaction proceeds, an imbalanced distribution of charge (electrons for inert metal electrodes) develops across the interface,

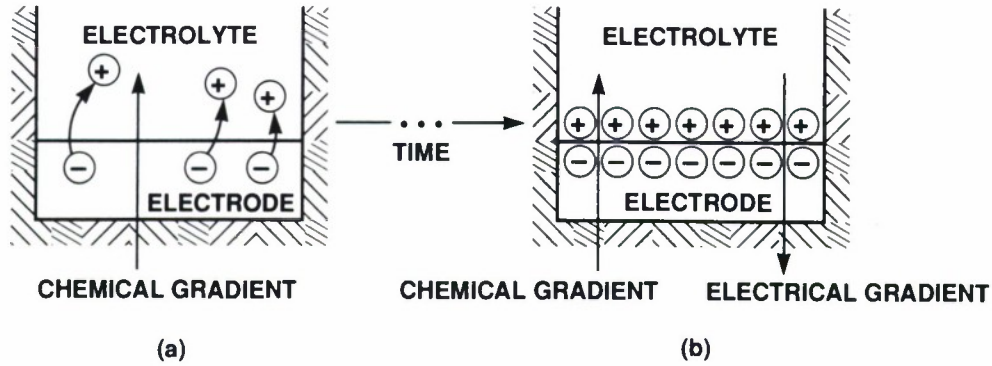


Figure 8. Formation of the electrical double layer from (a) initial reaction to (b) final equilibrium.

resulting in the formation of an electric field gradient that opposes the chemical gradient. Equilibrium is established when the electrical and chemical gradients are equal and opposite as shown in Figure 8(b). Here the reaction velocity reaches zero, preventing further charge movement. The trapped separation of charges at the interface (comprised of surface charge on the metal and diffuse countercharge of equal magnitude in the solution) constitute the high-impedance electric double layer [17].

Numerous attempts have been made to explain and model the electric double layer. Helmholtz modeled the double layer as an electrolytic capacitor with the double-layer potential given by

$$V(x) = \frac{\lambda}{\epsilon}(x - a) \quad 0 \leq x \leq a \quad (20)$$

where λ is the surface charge density, ϵ is the relative permittivity, and a is the width of the double layer (typically a few angstroms.) The voltage profile is shown in Figure 9(a). The capacitor model yields a linear drop in potential, with a magnitude of $\lambda a/\epsilon$ required to cross the double layer from the electrolyte to the electrode.

More complicated models allow a diffuse distribution of charge about the interface. For example, the Gouy-Chapman model avoids the unrealistic homogeneous anion and cation planar charge sheets used in the Helmholtz model by proposing several charge sheets, each having both cations and anions but of varying concentration. As shown in Figure 9(b), the charge sheets closest to the interface have a higher imbalance of charge, while the sheets furthest from the interface are electrically neutral. This double-layer potential is obtained by using Boltzmann statistics to characterize the charge density according to

$$\rho(x) = Z_+ F C_+^0 e^{-Z_+ F V(x)/RT} - Z_- F C_-^0 e^{-Z_- F V(x)/RT} \quad (21)$$

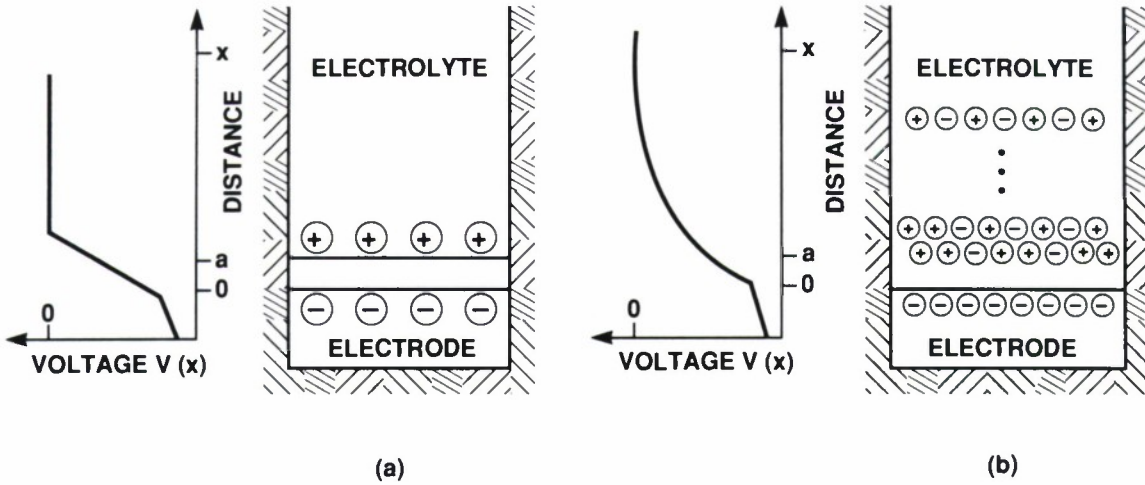


Figure 9. Voltage profiles of (a) Helmholtz and (b) Gouy-Chapman electric double-layer models.

where Z_+ and Z_- are the charge valences, F is the Faraday constant, C_+^0 and C_-^0 are the concentrations of the cations and anions, respectively, in the bulk solution, and R is the ideal gas constant. Substituting the linear approximation of (21) into the Poisson equation

$$\frac{\partial^2 V}{\partial x^2} = -\rho(x) / \epsilon \quad (22)$$

and solving the boundary conditions yields the double-layer potential given by

$$V(x) = -\frac{\sigma e^{\kappa a} e^{-\kappa x}}{\epsilon \kappa} \quad (23)$$

where

$$\kappa = \frac{F \sqrt{Z_+^2 C_+^0 + Z_-^2 C_-^0}}{\sqrt{\epsilon RT}} \quad (24)$$

Clearly, the length of the double layer depends on the ionic concentrations through κ , while the magnitude of the potential depends on both the surface charge and ionic concentrations. The mathematical difference between the earlier Helmholtz and current Gouy-Chapman models lies in the double-layer potential being exponential in distance from the interface, as shown in Figure 9(b). Although more complicated double-layer models exist, a complete understanding of the phenomenon and a corresponding precise mathematical model remain elusive.

Because a precise mathematical description of the double layer does not exist, empirical measurements are often incorporated into simple electrical circuit models to provide an accurate representation of the electrochemical processes. By performing a calibration experiment to determine the necessary em-

pirical parameters, the double layer can be satisfactorily modeled for electrode design purposes. The electrical circuit model employed consists of an electrolytic capacitor C_d in parallel with a leakage resistance R_d . Both components are allowed to vary in frequency to conform with empirical findings. The capacitor intuitively follows from the idealized Helmholtz model. However, by allowing the capacitor value to vary with frequency, together with the addition of the variable leakage resistor to account for the charge carriers realistically crossing the double layer, the parallel RC circuit is more representative of the Gouy-Chapman double-layer model.

Two methods can be used to obtain the double-layer equivalent circuit components R_d and C_d . The first involves relying on published results for conventional glass-coated bright platinum microelectrodes calibrated in physiological saline solution. Under such circumstances, both R_d and C_d have been found to vary as $\omega^{-1/2}$, while the impedance phase θ_d remains near -45° within the frequency band of interest (100 Hz-10kHz) [18,19]. Imposing these conditions upon the parallel RC model yields the relationships

$$\bar{Z}_d = \frac{R_d - j\omega R_d^2 C_d}{1 + (\omega R_d C_d)^2} \quad (25)$$

$$\theta_d = \tan^{-1} - \omega R_d C_d = -45^\circ \quad (26)$$

$$\therefore R_d = 1 / \omega C_d \quad (27)$$

where C_d is determined from published empirical results ($20\mu F/cm^2$ [16]).

An alternative method for obtaining the double-layer circuit components involves conducting an independent calibration experiment using the actual physiological saline solution used for the biochip neural experiments. This approach requires the calibration electrodes to be of the same metal and brightness as the microcircuit electrodes. When the conditions for employing the biochip differ from published experiments, the following calibration experiment will provide accurate double-layer modeling.

The calibration experiment described enables isolation of the required circuit components R_d and C_d by providing a macroscopic environment where other electrical effects become negligible. The calibration tube used is shown in Figure 10(a). The calibration macroelectrodes are gold plated, of similar brightness as the microelectrodes in the biochip; the macroelectrodes are connected to a precision impedance analyzer (HP 4284A) through a four-terminal pair configuration. This configuration minimizes unwanted residual factors arising from self and/or mutual inductance between the individual leads. Because both open- and short-circuit measurements are made prior to the calibration, no stray impedance from the leads is introduced. The glass tube is long enough so that the electrode-to-electrode capacitance can be ignored. Consequently, the circuit schematic shown in Figure 10(b) provides sufficient representation.

The specific objective of the calibration experiment is to calculate the calibration components C_d° and R_d° from the overall impedance measurements (Z°) performed at various frequencies of interest. This overall impedance can be expressed

$$\bar{Z}^\circ \equiv Z^\circ \angle \theta^\circ \equiv R^\circ + jX^\circ = \left(2R_s^\circ + \frac{2R_d^\circ}{\alpha} \right) + j \left(-2\omega (R_d^\circ)^2 \frac{C_d^\circ}{\alpha} \right) \quad (28)$$

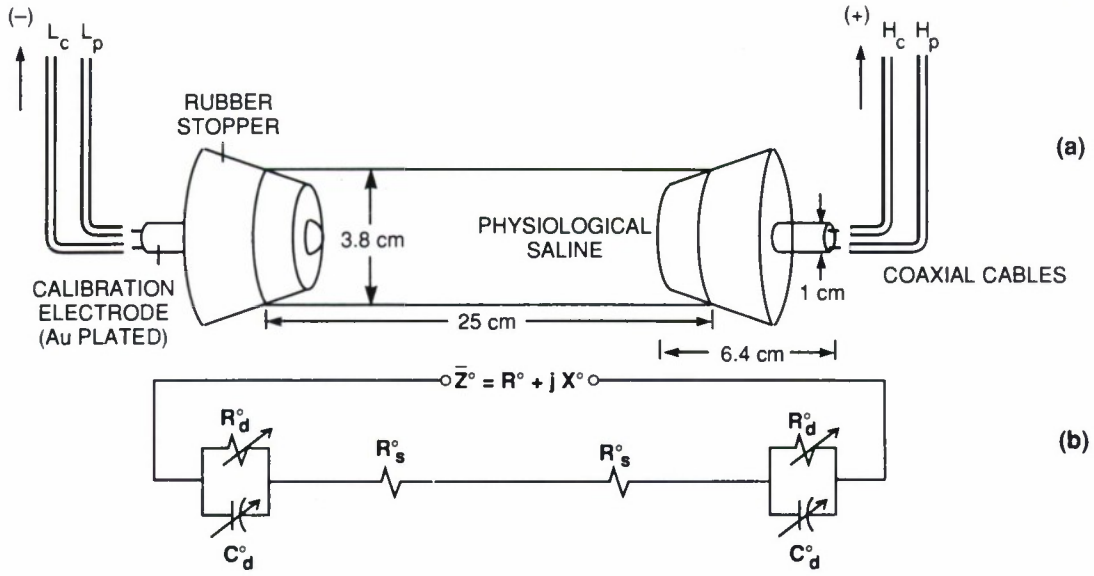


Figure 10. Diagram of (a) calibration experiment and (b) equivalent circuit.

where $\alpha = 1 = (\omega R_d^\circ C_d^\circ)^2$ and the spreading resistance for the calibration electrode is $R_s^\circ = \rho / 2\pi r^\circ$. Hence, C_d° and R_d° are easily obtained from (28) in terms of the measured resistance and reactance, as

$$C_d^\circ = \frac{-2X^\circ}{\omega \left((R_e^\circ)^2 + (X^\circ)^2 \right)} \quad (29a)$$

$$R_d^\circ = \frac{(R_e^\circ)^2 + (X^\circ)^2}{2R_e^\circ} \quad (29b)$$

where

$$R_e^\circ = R^\circ - 2R_s^\circ \quad (30)$$

In turn, the microcircuit double-layer component C_d is computed by

$$C_d = C_{d/A}^\circ A_c \quad (31)$$

where $C_{d/A}^\circ = C_d^\circ / 2\pi(r^\circ)^2$ is the capacitance normalized to the calibration macroelectrode surface area and A_c is the microelectrode surface area. Finally, the leakage resistance for the microelectrode is computed by

$$R_d = -\tan \theta_d^\circ / \omega C_d \quad (32)$$

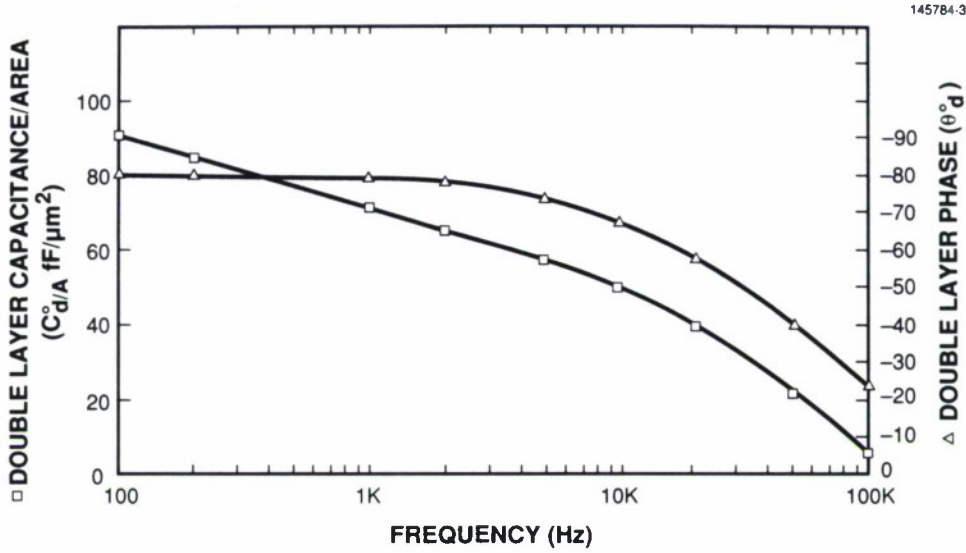


Figure 11. Experimental calibration constants.

The results of the calibration experiment using the specific neural growth solution employed in subsequent neural experiments are shown in Figure 11. Consequently, knowing both the double-layer capacitance per area ($C_{d/A}^o$) and the phase θ_d^o , the necessary double-layer components R_d and C_d are easily computed for the frequencies of interest.

R_l —Line Resistance

The resistance R_l of the metal conductor carrying current from the electrode to the microcircuit bonding pad comprises two components; the first from the adhesive titanium layer, the second from the gold conductor, as shown in Figure 12. Hence, the line resistance for the double-layered conductor becomes

$$R_l = \frac{V}{i_1 + i_2} = (R_1^{-1} + R_2^{-1})^{-1} = \frac{\rho_1 \rho_2}{D_{l_2} \rho_1 + D_{l_1} \rho_2} \cdot \frac{L_l}{W_l} \quad (33)$$

since

$$R_i = \rho_i L_l / W_l D_{l_i} \quad (34)$$

where ρ_1 and ρ_2 are the resistivities of the adhesion and conductor layers, respectively, L_l and W_l are the length and width of the electrode line, and D_{l_1} and D_{l_2} are the depths of the respective layers comprising the electrode line.

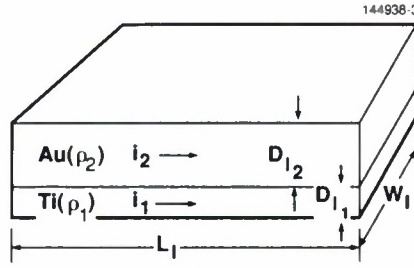


Figure 12. Electrode line with conducting and adhesion layers.

C_s — Shunt Capacitance

The capacitance C_s accounts for the current shunted from the electrode line to ground. As diagrammed in Figure 13, this shunt capacitance is modeled as a parallel-plate capacitor, with the metal electrode line representing the bottom plate and the electrolyte solution representing the upper conducting plate. A first approximation for the shunt capacitance excludes the fringing effects arising from the upper plate (electrolyte) exceeding the dimension of the lower plate (electrode line). Therefore, the flux generated by the dashed electric field lines shown in Figure 13 is discounted. With such approximation, the shunt capacitance becomes

$$C_s = \frac{k\epsilon_0 L_l W_l}{D_i} \quad (35)$$

where k is the relative dielectric constant, ϵ_0 is the permittivity of free space, L_l and W_l are the length and width of the electrode line under the electrolyte, respectively, and D_i is the depth of the insulating dielectric. Although (35) is a first approximation, the model suffices, as the shunt capacitance will be shown to be insignificant in comparison to the dominant double-layer impedance.

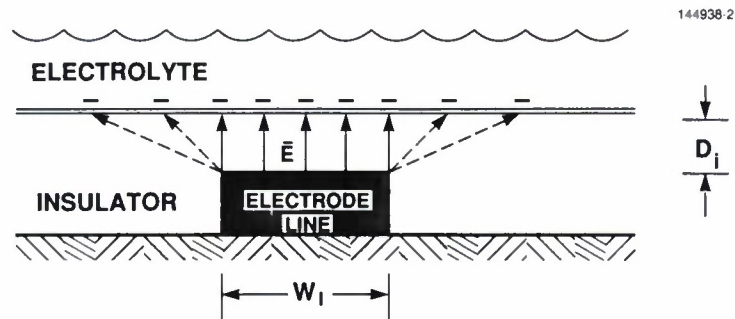


Figure 13. Cross-section of shunt capacitance between the electrode and electrolyte.

The microcircuit electrode equivalent circuit is now complete; the components are summarized in Table 1. The electrical characteristics are expressed as a function of the electrode dimensions labeled in Figure 14. To understand the relative magnitudes of the various components, consider two gold square-electrode designs enumerated in Table 2. The impedances are calculated at a frequency of 1 kHz, since typical neuronal signals occur in the 100-Hz to 10-kHz bandwidth.

TABLE 1
Microcircuit Electrode Equivalent Circuit

| Component (1 kHz) | Model | Typical Values | |
|---------------------------|--|--|--|
| | | 10 $\mu\text{m} \times 10 \mu\text{m}$ | 50 $\mu\text{m} \times 50 \mu\text{m}$ |
| Spreading Resistance | $R_s = \frac{\rho}{W_c \sqrt{4\pi H/D}}$ | 35.4 k Ω | 7.08 k Ω |
| Electrode Line Resistance | $R_l = \frac{\rho_1 \rho_2}{\left(D_{l_2} \rho_1 + D_{l_1} \rho_2\right)} \frac{L_l}{W_l}$ | 1.62 k Ω | 1.62 k Ω |
| Double-Layer Capacitance | $C_d = C_{d/A} A_c \quad (\theta_d = 45^\circ)$ | 20 pF | 500 pF |
| | $C_d = C_{d/A}^\infty A_c \quad (\text{calibration})$ | 7.16 pF | 179 pF |
| Double-Layer Resistance | $R_d = 1/\omega C_d \quad (\theta_d = 45^\circ)$ | 7.96 M Ω | 318 k Ω |
| | $R_d = -\tan \theta_d / \omega C$ | 117 M Ω | 4.66 M Ω |
| Shunt Capacitance | $C_s = \frac{k\epsilon_0 L_l W_l}{D_i}$ | 3.84 pF | 3.84 pF |

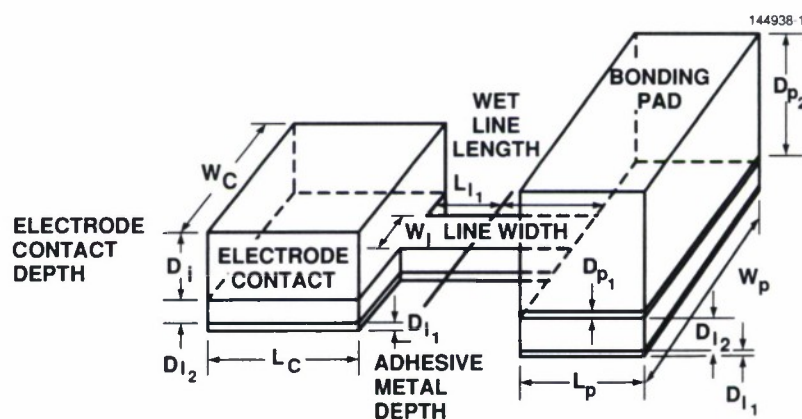


Figure 14. Dimension labeling of microcircuit electrode.

TABLE 2
Dimensions for Plausible Electrode Designs
Microcircuit Electrode Design

| Dimension | | Design 1 10 μm \times 10 μm | Design 2 50 μm \times 50 μm |
|--------------|--|---|--|
| W_c | Width of Electrode Contact | 10 μm | 50 μm |
| L_c | Length of Electrode Contact | 10 μm | 50 μm |
| D_{l_2} | Depth of Electrode Line and Contact Conductor Metal | 500 \AA | 500 \AA |
| D_{l_1} | Depth of Electrode Line and Contact Adhesion Metal | 100 \AA | 100 \AA |
| D_i | Depth of Recessed Electrode Contact | 4000 \AA | 4000 \AA |
| W_l | Width of Electrode Line | 5 μm | 5 μm |
| L_{l_1} | Length of Electrode Line in Electrolyte Area | 8 mm | 8 mm |
| L_{l_2} | Length of Electrode Line in Dry Area | 10 mm | 10 mm |
| L_l | Length of Total Electrode Line | 18 mm | 18 mm |
| D_ρ | Depth of Bonding Pad Conductor | 1 μm | 1 μm |
| D_ρ^2 | Depth of Bonding Pad Adhesive Metal | 500 \AA | 500 \AA |
| L_p^1 | Length of Bonding Pad | 10 mil | 10 mil |
| W_p | Width of Bonding Pad | 10 mil | 10 mil |
| H | Height of Metal Ground Ring | 5 mm | 5 mm |
| D | Diameter of Metal Ground Ring | 15 mm | 15 mm |
| Constants | | Values | |
| ρ | Neural Solution Resistivity | $72.5 \times 10^{-2} \Omega \cdot \text{m}$ | |
| ρ_1 | Titanium Resistivity | $42 \times 10^{-8} \Omega \cdot \text{m}$ | |
| ρ_2 | Gold Resistivity | $2.27 \times 10^{-8} \Omega \cdot \text{m}$ | |
| $C_{d/A}$ | Capacitance Density | 0.2 pF/ μm^2 | |
| f | Frequency | 1 kHz | |
| k | S_iO_2 Dielectric Constant | 4.34 | |
| ϵ_0 | Permittivity | $8.85418 \times 10^{-12} \text{ coul}^2/\text{nt} \cdot \text{m}^2$ | |

The corresponding component values are displayed in Table 1. The double layer accounts for most of the impedance contribution; this is where the two designs differ substantially. Therefore, the area of the electrode tip, which determines the double-layer impedance through C_d and R_d , is an influential factor in the electrode design.

2.2.2 System Impedance Calculation

To define a cost function for the microcircuit electrode design, the system impedance of the previously derived equivalent circuit [Figure 6(c)] must be obtained. This theoretical impedance function is a convenient benchmark for subsequent evaluation of fabricated biochips. Therefore, system impedance is instrumental in both design and evaluation.

The system impedance of the equivalent microcircuit electrode submerged in a homogeneous conducting medium is composed of two impedances in parallel, as indicated in Figure 15.

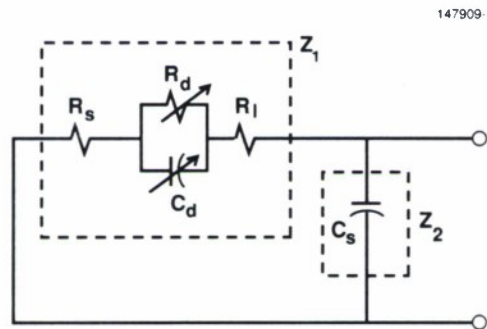


Figure 15. Impedance reduction of equivalent circuit.

Combining the impedances using relations previously obtained,

$$\bar{Z}_1 = R_s + R_l + \bar{Z}_d \quad (36)$$

and

$$\bar{Z}_2 = -j / \omega C_s \quad (37)$$

where

$$\bar{Z}_d = \frac{R_d - j\omega C_d R_d^2}{1 + (\omega C_d R_d)^2} \quad (38)$$

The system impedance then becomes

$$\bar{Z} \equiv R + jX = \frac{\alpha R_e}{\beta^2 + (\omega C_s R_e)^2} - j \frac{\omega (C_s R_e^2 + \beta C_d R_d^2)}{\beta^2 + (\omega C_s R_e)^2} \quad (39)$$

or, in polar form,

$$Z = |\bar{Z}| = \sqrt{(\alpha R_e)^2 + \omega^2 (C_s R_e^2 + \beta C_d R_d^2)^2} \quad \left(\beta^2 + (\omega C_s R_e)^2 \right) \quad (40)$$

$$\theta = \angle \bar{Z} = \tan^{-1} \left(-\omega (C_s R_e^2 + \beta C_d R_d^2) / \alpha R_e \right) \quad (41)$$

where

$$\alpha = 1 + (\omega C_d R_d)^2 \quad (42)$$

$$\beta = 1 + \omega^2 R_d^2 C_d (C_d + C_s) \quad (43)$$

$$R_e = (R_s + R_l) \alpha + R_d \quad (44)$$

The system impedance (39) can be expressed as a function of all relevant microcircuit electrode dimensions by substituting in the previously derived circuit component equations [(19),(31-33),(35)] as summarized in Table 1. This net collection of equations can be set into a computer program to provide an efficient system impedance calculation, given any microcircuit electrode dimensions. The following approximations to the system impedance function allow rapid calculations in the absence of a computer.

In most practical microcircuit electrode designs, the double-layer components dominate the system impedance. By assuming $C_d \gg C_s$ and $R_d \gg (R_s + R_l)$, α , the system impedance (40) reduces to

$$\begin{aligned} Z'' &= \sqrt{(\alpha R_d)^2 + \omega^2 [R_d^2 (\beta C_d + C_s)]^2} / \left(\alpha^2 + (\omega C_s R_d)^2 \right) \\ &\cong \alpha R_d \sqrt{1 + \omega^2 C_d^2 R_d^2} / \left(\alpha^2 + (\omega C_s R_d)^2 \right) \\ &\cong \frac{\alpha R_d \sqrt{\alpha}}{\alpha^2} \\ &= R_d / \sqrt{\alpha} \\ &= R_d / \sqrt{1 + (\omega R_d C_d)^2} \end{aligned} \quad (45)$$

with phase

$$\begin{aligned} \theta'' &= \tan^{-1} \left(-\omega R_d^2 (\beta C_d + C_s) / \alpha R_d \right) \\ &\cong \tan^{-1} \left(-\omega R_d^2 \alpha C_d / \alpha R_d \right), \quad \alpha \cong \beta \\ &= \tan^{-1} \left(-\omega R_d C_d \right) \end{aligned} \quad (46)$$

Note that under this assumption, the system impedance function reduces to a parallel RC circuit where only the double-layer components contribute.

Another reduction follows, derived from assuming similar conditions supporting published results obtained using conventional glass-coated bright-platinum microelectrodes calibrated in physiological saline solution. Here C_d and R_d also dominate the system impedance, but in addition the double-layer phase remains constant at $\theta_d = 45^\circ$ [16]. Specifically, by assuming $C_d \gg C_s$, $R_d \gg (R_s + R_l)$ and $\theta_d = \tan^{-1} - \omega R_d C_d = -45^\circ$, the impedance (40) reduces to

$$\begin{aligned} Z' &= \sqrt{4R_d^2 + \omega^2 \left[R_d^2 (2C_d + C_s) \right]^2} / \left(4 + (\omega C_s R_d)^2 \right) \\ &\cong 2R_d \sqrt{1 + \omega^2 C_d^2 R_d^2} / 4 \\ &= R_d / \sqrt{2} \end{aligned} \quad (47)$$

with phase

$$\begin{aligned} \theta' &= \tan^{-1} \left(-\omega (R_d^2 2C_d) / 2R_d \right) \\ &= \tan^{-1} (-\omega R_d C_d) = -45^\circ \end{aligned} \quad (48)$$

The original system impedance function (39) and the approximate forms (45-48) will be compared to actual biochip electrode measurements in the ensuing evaluation (section 2.4.1).

2.2.3 Design Optimization

To optimize the microcircuit electrode design, a cost function is defined in terms of the previously derived equivalent circuit components. That cost function is the signal-to-noise ratio (SNR) defined across the microcircuit electrode bonding pad and ground terminal (as indicated by the open terminals in Figure 15). Mathematically optimizing this cost function is equivalent to selecting the electrode dimensions that provide the largest received electrode signal, given the present noise. This SNR is expressed as

$$SNR = P_S / P_N \quad (49)$$

where P_S is the average signal power and P_N is the average noise power, both derived below.

The limiting biochip noise source is thermal noise (Johnson noise) arising from the random motion of charge carriers. This noise is a function of the resistive component of the equivalent system impedance derived previously. Therefore, the Nyquist thermal noise power expression for the biochip electrode is

$$P_N = 4kT\Delta_f R \quad (50)$$

where $k = 1.38 \times 10^{-23} \text{ J/K}$ (Boltzmann's constant), T is the operating temperature in K , Δ_f is the signal bandwidth in Hz , and R is the resistive portion of the system impedance (39) in ohms.

The average signal power is easily obtained by realizing that the equivalent circuit (Figure 6c) is simply a voltage divider, with the output signal voltage in phasor form given by

$$\bar{V} = A \bar{V}_s \quad (51)$$

with A the attenuation

$$\bar{A} = \frac{\bar{Z}_2}{\bar{Z}_1 + \bar{Z}_2} = \frac{1}{1 + j\omega C_s (R_1 + jX_1)} \quad (52)$$

and $Z_1 \equiv R_1 + jX_1$. The attenuation magnitude is

$$A \equiv |\bar{A}| = \left[\left(1 - \omega C_s X_1 \right)^2 + \left(\omega C_s R_1 \right)^2 \right]^{-\frac{1}{2}} \quad (53)$$

while the resistive portion of the system impedance can be expressed as

$$\begin{aligned} R &= \text{Re} \left\{ \frac{R_1 + jX_1}{(1 - \omega C_s X_1) + j(\omega R_1 C_s)} \right\} \\ &= \frac{R_1}{(1 - \omega C_s X_1)^2 + (\omega R_1 C_s)^2} \\ &= A^2 R_1 \end{aligned} \quad (54)$$

Substitution of (51) and (50) into (49) yields the SNR expression

$$\begin{aligned} \text{SNR} &= \frac{|\bar{V}|^2}{4kT\Delta_f R} \\ &= \frac{A^2 V_s^2}{4kT\Delta_f A^2 R_1} \\ &= \frac{V_s^2}{4kT\Delta_f R_1} \end{aligned} \quad (55)$$

where

$$\begin{aligned} R_1 &= R_s + R_l + \frac{R_d}{1 + (\omega C_d R_d)^2} \\ &= R_s + R_l + \frac{R_d}{1 + \tan^2 \theta_d} \end{aligned} \quad (56)$$

Optimizing the SNR design cost function (55) corresponds to minimizing the double-layer resistance term $R_d/(1+\tan^2\theta_d)$, since typically $R_d \gg (R_s + R_l)$ and both the temperature and bandwidth are fixed. In turn, minimization of the double-layer resistance term corresponds to maximizing the electrode surface area A_c , because for the first method outlined for obtaining R_d (using a published value of $C_{d/A}$ and $\theta_d = -45^\circ$)

$$\text{SNR}' = \frac{2V_s^2 \omega C_{d/A}}{4kT\Delta_f} A_c \quad (57)$$

while the second method (based on the calibration experiment where $C_{d/A}^\circ$ and θ_d° are measured)

$$SNR'' = \frac{(1 + \tan \theta_d^\circ) V_s^2 \omega C_{d/A}^\circ}{4kT\Delta_f \tan \theta_d^\circ} A_c \quad (58)$$

The SNR is independent of the electrode line insulation depth D_i . Therefore, the primary constraint governing the depth selection is the insulator breakdown voltage ($V_{bd} = 1.6\text{mV}/\text{\AA}$ for quartz). Layering of the insulation layer provides additional immunity against migration of sodium ions.

As a consequence, an optimal microcircuit electrode design using conventional fabrication techniques simply corresponds to choosing the electrode surface area A_c as large as possible. An upper bound for the area is determined by the density of the connecting neurons; too large an electrode will invite crosstalk from neighboring neurons. Typically, the electrode area is designed to be approximately the size of the neuron to avoid unwanted crosstalk in modest-density networks (neuron to neuron spacing about 2-5 cell bodies). The resulting design dimensions for the microcircuit electrode for rat neurons (10 μm diameter) and Aplysia neurons (50 μm diameter) are given in Table 1.

Significant performance enhancement can be achieved by employing unconventional fabrication techniques. As observed from the SNR expressions (57) and (58), electrode design optimization employing conventional fabrication techniques requires maximizing the surface area of the electrode contact. However, the footprint of the electrode contact is restricted to the size of the neural cell body to avoid crosstalk from neighboring neurons. Further increasing the SNR requires increasing the surface area while maintaining a fixed electrode footprint of the order of the cell body size. An unconventional solution (borrowed from the biology community) to this constrained optimization problem entails electrically platinizing the microcircuit electrodes to create a rough, porous surface several times greater in surface area than its footprint. The effect of platinizing on the SNR can be formulated by considering the new platinized surface area to be

$$A_p = \gamma A_c \quad (59)$$

which results in the new SNR

$$SNR_{plat} = \gamma SNR \quad (60)$$

or in decibels

$$SNR_{plat} = SNR(\text{dB}) + 10 \log \gamma \quad ; \quad (61)$$

an increase of $10 \log \gamma(\text{dB})$ in SNR results. For example, with a value of $\gamma = 100$, the SNR is theoretically improved by 20dB, as will be demonstrated experimentally in a subsequent evaluation section.

Although mathematically optimal electrodes can be designed as discussed, the actual behavior of the electrode surrounded by neural tissue will vary from prediction. The deviation is attributed to the complex pattern of ionic currents that develops surrounding each of the current-generating neurons. Consequently, the modeling and subsequent design optimization based on a homogeneous conducting

medium (such as isotonic saline solution) provides insight and general design guidelines, but should not be taken as an accurate representation of experimental conditions surrounding nonhomogeneous neural networks.

2.2.4 Bipolar Electrode Design

The previous design sections provide techniques for designing microcircuit electrodes which exhibit good recording performance (high SNR). However, additional considerations must be addressed to provide both extracellular recording and stimulation capability. Without such additional considerations, stimulation can be achieved only in a global manner using the previously designed recording electrodes; that is, the electric field developed when a stimulus voltage is applied across a single recording electrode and the ground terminal irradiates the entire electrode array. Thus, all neurons within the network are significantly influenced when an attempt is made to stimulate a single neuron resting above a given electrode. To provide focused or localized stimulation, where only a single neuron is effected, the following bipolar electrode design criteria are presented.

The first bipolar design, shown in Figure 16(a), is a combination of two recording electrodes, one serving as the anode, the other as the cathode. This represents the simplest bipolar design. An alternative design is shown in Figure 16(b). Although more complex, this circular design yields an electric field that is radially symmetric from anode to cathode. Here the electric stimulation induced is uniform with respect to the neural cell body centered over the circular electrode, contributing to more efficient stimulation.

Specifically, the additional design considerations center about the gaps between the anode and cathode, and between the paired electrode lines. These small dielectric gaps, which separate two conductors, can induce unwanted capacitance and cause dielectric breakdown if the stimulus voltage is excessive. Hence, both of these adverse effects must be quantitatively addressed in the design of bipolar electrodes.

The capacitance induced by the gap between the electrode lines can be approximated by assuming a parallel-plate-capacitor model. The resulting upper bound for the length of the paired electrode lines of depth D_p , separated by a gap of size W_g , is

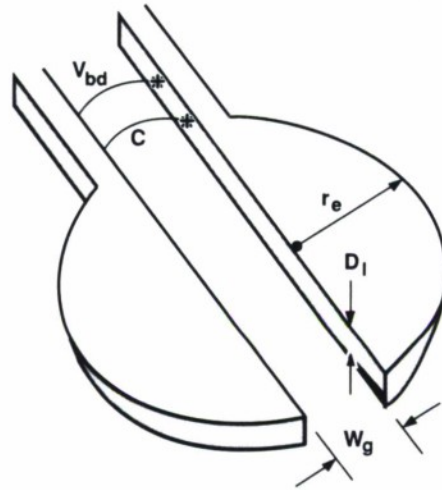
$$L_{\max} = \frac{W_g C_{\max}}{k\epsilon_0 D_l} \quad (62)$$

where C_{\max} is the maximum capacitance allowed (typically about 1pF). The additional capacitance between the anode and cathode for the circular bipolar design can be similarly approximated by assuming an ideal cylindrical-capacitor model. The resulting lower bound for the cathode/anode diameter ratio is

$$\left. \frac{r'_c}{r_a} \right|_{\min} = e^{\frac{2\pi k\epsilon_0 D_l}{C_{\max}}} \quad (63)$$

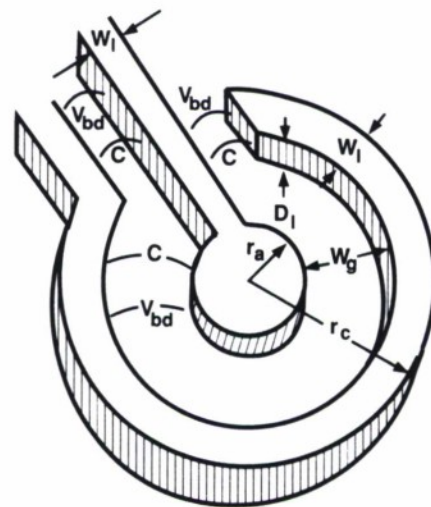
where $r'_c = r_c - W_l$ is the cathode inner radius, r_a is the anode outer radius, and C_{\max} is again the maximum capacitance allowable.

147663-4



(a)

147663-3



(b)

Figure 16. Diagram of (a) simple and (b) circular bipolar electrodes.

The remaining adverse effect to be addressed is the dielectric breakdown caused by excessive voltage levels during stimulation. The dielectric breakdown voltage is given by

$$V_{bd} = \xi d \quad (64)$$

where ξ is the dielectric strength (1.6mV/Å for quartz) and d is the distance across the gap of interest. Knowing the maximum voltage required for stimulation (typically less than 1 volt), the minimum allowable gap distance is easily computed. Several calculations must be made to determine the minimum distances for the electrode line-pair gap, electrode line-to-electrolyte gap (D_i), and the anode-to-cathode gap (W_g).

Conforming to these design guidelines, a bipolar test chip containing an array of 36 bipolar electrodes (10 simple, 24 circular, and 2 diagnostic) was designed; the results are tabulated in Table 3. Both the gap width and electrode diameter for the simple design were varied within the acceptable limits. The circular designs exhibit variation in both anode and cathode diameters. These variations enable empirical determination of the best stimulus design for a cell approximately 50µm in diameter.

TABLE 3
Simple and Circular Bipolar Design Dimensions

| Simple Design (D_e/W_g ratios shown) | | | |
|---|---|-------|-------|
| Gap Width (W_g) | Diameter of Electrode (D_e) | | |
| | 20 µm | 30 µm | 50 µm |
| 5 µm | 4:1 | 6:1 | 10:1 |
| 10 µm | 2:1 | 3:1 | 5:1 |
| 15 µm | | 2:1 | 3.3:1 |
| 20 µm | | | 2.5:1 |
| 25 µm | | | 2:1 |
| Circular Design (D_c/D_a ratios shown) | | | |
| Anode Diameter (D_a) | Cathode Diameter (D_c) | | |
| | 40 µm | 60 µm | 85 µm |
| 10 µm | 4:1 | 6:1 | 8.5:1 |
| 14 µm | 2.9:1 | 4.3:1 | 6.1:1 |
| 20 µm | 2:1 | 3:1 | 4.3:1 |
| 30 µm | | 2:1 | 2.8:1 |
| 40 µm | | | 2.1:1 |

2.3 MICROCIRCUIT ELECTRODE ARRAY FABRICATION

Conventional microfabrication techniques together with biologically compatible substrates were employed to fabricate the previously designed biochip electrode arrays. These materials and the accompanying fabrication methods are detailed in the following sections. Fabrication results for both unipolar and bipolar electrode arrays will be detailed.

2.3.1 Material Selection

Material considerations specific to interfacing fabricated microcircuits and living cells must be addressed to avoid cell contamination and biochip deterioration. Electrode deterioration can be minimized by choosing non-corrosive inert metals such as gold, which has good, stable electrical conduction properties. The effectiveness of the insulator can deteriorate due to the persistent migration of sodium ions present in the physiological saline bath. Methods to curb insulator deterioration include choosing materials such as silicon nitride, which is resistant to sodium migration, and layering the insulator material, to cover possible submicron pits formed during fabrication of each layer. Although single-layer silicon dioxide can be used, it degrades within a few months.

Many of the common microfabrication substrates are suitable for cell growth. Successful neural growth has been achieved on glass, silicon, and silicon dioxide (quartz). Quartz is favored because the clear substrate allows neural experimentation to be viewed with a transmission microscope, and the material is dimensionally stable at the high temperatures required for processing. Finally, by choosing three-inch diameter quartz wafers, four biochips per wafer can be attained.

2.3.2 Fabrication Methods

Fabrication begins by cleaning the 15-mil thick quartz wafers by ultrasonic agitation in a detergent bath for 15 minutes. Further cleaning is done by a plasma etcher (97% helium, 3% oxygen) for one minute.

The basic procedure for biochip fabrication following cleaning is illustrated in Figure 17. The electrode pattern is made by first treating the chosen substrate with an adhesion promoter. A solution of 50% hexamethyldisilazane (hmbs) and 50% xylene is puddled on and allowed to sit for 10 seconds. The substrate is then spun at 3000 rpm to remove all but a monolayer of hmbs. One-half micron of positive photoresist (Shipley S1805) is then spun onto the wafer and baked for 30 minutes at 90°C in flowing air. Next, the substrate is placed in vacuum contact with a 60-mil thick glass mask bearing the electrode pattern in an ultraviolet (UV) opaque material. The photoresist is exposed to UV light through this mask. The substrate is then dipped in developer to remove the photoresist which has been exposed to the light. This leaves photoresist everywhere except on the electrode pattern. Using an electron beam evaporator, 100 angstroms of titanium are then deposited onto the substrate, followed by 500 angstroms of gold. The photoresist is removed in acetone, removing the metal that has been deposited on the surface, leaving only the electrode pattern in gold.

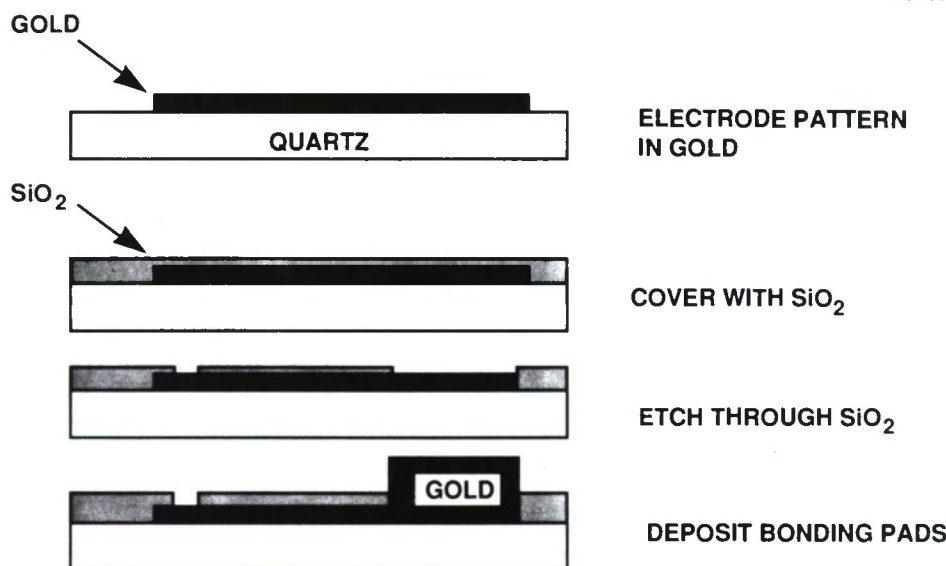


Figure 17. Biochip fabrication procedure.

Next, the dielectric insulation layer is deposited. Depending on the design, 2000 to 4000 angstroms of silicon dioxide (SiO_2) is deposited using chemical vapor deposition. After covering the entire surface with SiO_2 , holes are cut to expose the ends of the electrodes. The substrate is coated with one-half micron of photoresist and baked as before. Using a contact aligner, the photoresist is exposed with the hole pattern aligned to the electrode pattern. After developing the SiO_2 is etched through in a plasma etcher using a mixture of CF_4 and O_2 and using the photoresist as a mask. The photoresist is then removed in ACT-1 resist stripper at 90°C .

The outer ends of the electrodes are coated with 1 μm of gold for final package bonding. First, the substrate is coated with 3 μm of photoresist (Shipley 1375) and baked at 90°C for 45 minutes in flowing air. Next, the bonding pad pattern is UV exposed using a contact aligner and developed. Here 500 angstroms of titanium and 1 μm of gold are electron-beam evaporated onto the substrate. The excess titanium and gold are then removed by dissolving the photoresist in acetone.

The microcircuit is ready for packaging into a 72-lead gold-plated package, with a hole in the back for microscopic viewing. The four circuits on a wafer are cut apart using a diamond saw. After being epoxied into the package, the package leads are wire bonded to the bonding pads, using gold wire. A gold-coated ring is epoxied to the center of the circuit to isolate the growth solution and act as the ground connection for electrical measurements.

To further reduce electrode impedance and boost SNR, platinization can be performed. Platinization is conducted by passing a DC current through the electrodes while immersed in Kohlrausch's [20] platinum chloride solution. The magnitude and duration of the current controls the amount of platinum

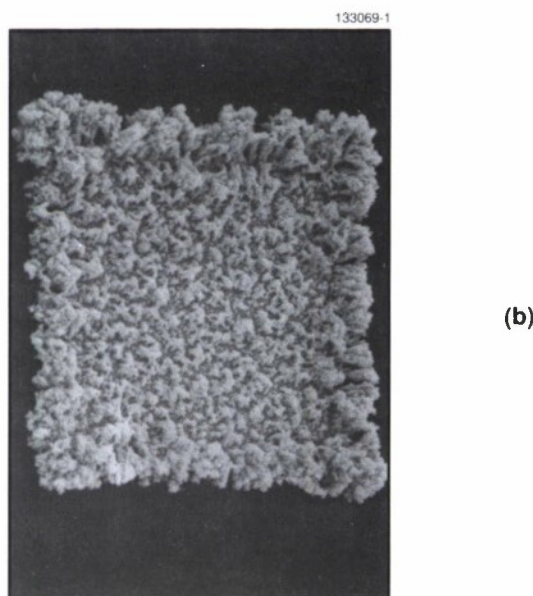
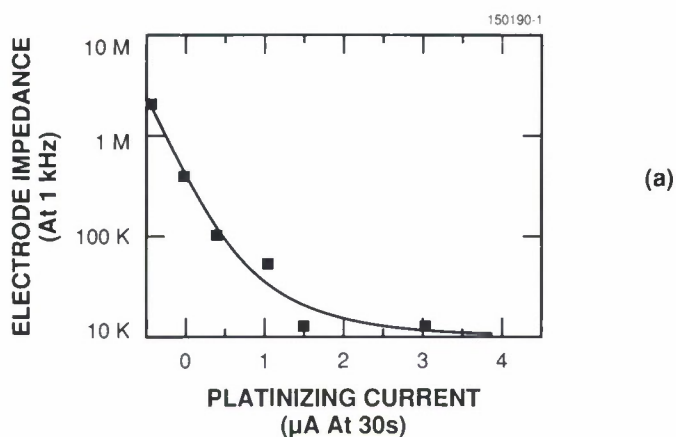


Figure 18. Electrode (a) impedance and (b) colloidal surface layer following platinization.

deposited. Larger platinum electrode deposits warrant lower impedances, but are undesirably delicate, so the current is largely set by empirical findings that substantiate firm platinum deposits at the expense of higher impedance. The best platinization conditions observed are shown in Figure 18(a), where a platinization current of $2\ \mu\text{A}$ for 30 seconds reduces electrode impedance by approximately two orders of magnitude, simultaneously providing a firm platinum deposit as indicated by the electron micrograph shown in Figure 18(b).

2.3.3 Fabrication Results

Typical results from a good fabrication run are displayed. A picture of the unipolar electrode array is shown in Figure 19(a), with the outside dimensions approximately one-inch square with 18 bonding pads per side. The pattern of 5 μm -wide lines converges to the small electrode array shown in Figure 19(b). The array contains 72 electrodes spaced 50 μm apart.

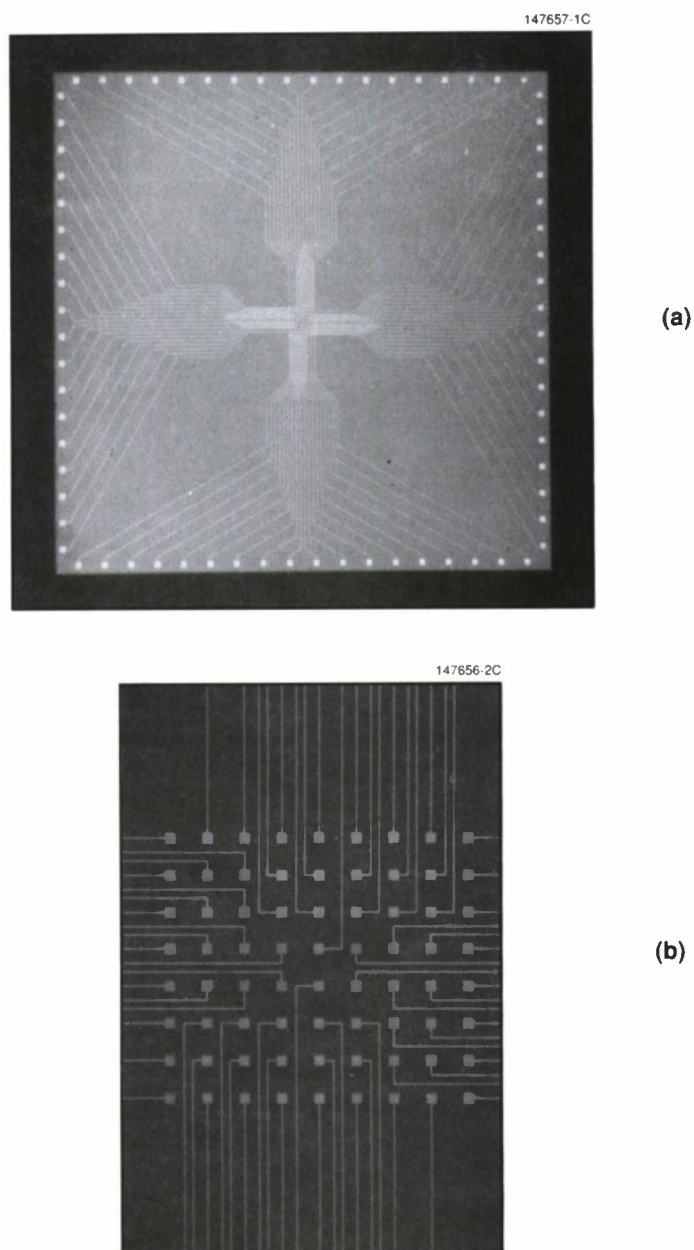
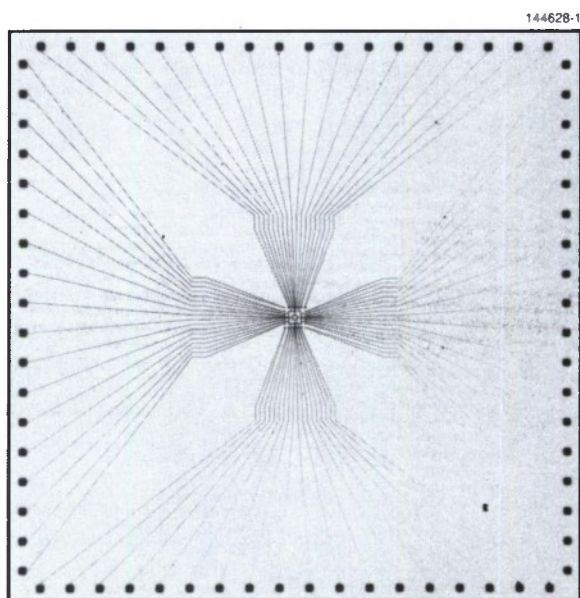
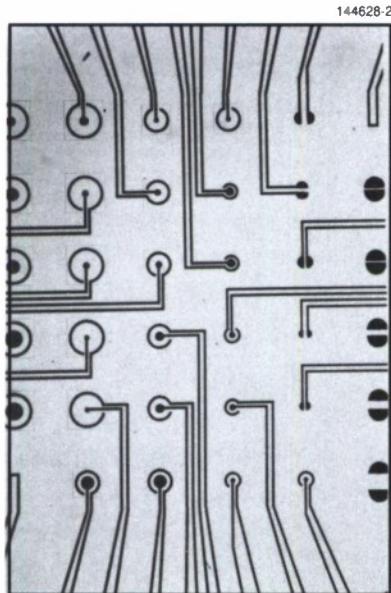


Figure 19. Unipolar (a) biochip with (b) 72-electrode array.

Figure 20 shows the bipolar electrode array with similar outside dimensions and bonding sites. This array contains 34 bipolar electrodes spaced $250\text{ }\mu\text{m}$ apart.



(a)



(b)

Figure 20. Bipolar (a) biochip with (b) 34-electrode array.

2.4 MICROCIRCUIT ELECTRODE ARRAY EVALUATION

Once fabricated, the biochips are visually inspected and quantitatively evaluated based on the system impedance measurements. The evaluation consists of comparing the measurements, taken as prescribed in the following section, to the theoretical impedance function (derived in section 2.2.2). Biochips with impedance values favorably correlated to theoretical prediction and possessing a low standard deviation across the 72 electrodes in the array are designated for neuronal experimentation.

2.4.1 Impedance Measurements

The measurement session begins by setting the test voltage amplitude and frequency and conducting open- and short-circuit calibration tests using the precision impedance analyzer (HP 4284 A). Specifically, the sinusoidal test voltage level must be low (approximately 25 mV) to avoid insulator breakdown above the electrode lines. The frequency can be varied in the band of interest; however, the impedance values at 1 kHz are the most informative, as such a frequency is commensurate with the neural action potential bandwidth. Measurements are taken by filling the neural reservoir with neural growth solution, then clamping the ground test lead to the biochip electrode lead of interest. The magnitude and phase measurements are recorded sequentially.

Evaluation results from the best fabrication run (565 electrodes were operable among 8 biochips) are tabulated in Table 4. Both theoretical and measured impedance values are shown. The exact impedance function (40) and the first approximation function that incorporates the calibration results (45) yields approximately the same values (2% difference), while the other approximation method (47) is significantly different (74% difference). The discrepancy is attributed in part to the neural growth solution used and the gold electrode metal. Both are different from those substances used in the published calibration experiment from which $C_{d/A}$ was obtained [16]. When comparing the measured values to the exact and first-approximation theoretical results, a good conformance is displayed, especially at 1 kHz where less than 7% difference is reported. Notice that the standard deviation among the 565 electrodes for the measurements taken at 1 kHz is approximately 10%, while the deviation increases to 18% at 100 Hz. The difference in deviations is due to both the sampling size being smaller at 100 Hz (71 electrodes) and the credibility loss in the double-layer model at low frequencies. The overall evaluation is graphically displayed in Figure 21, where the impedance (both theoretical and empirical) is seen to display the characteristic $\omega^{-1/2}$ behavior.

As a result of the measurements given previously, the evaluation results substantiate the electrode modeling approach based on the calibration experiment from which the electrical double-layer components are obtained. Also, the use of the first-approximation impedance function (45) appears warranted.

TABLE 4
Theoretical and Measured Biochip Electrode Impedances

| Impedance (M Ω) | Frequency (Hz) | | |
|-------------------------|--|---|--|
| | 100 | 1 k | 10 k |
| Theoretical | | | |
| Exact | 6.76 \angle -79.8° | 0.857 \angle -79.8° | 0.118 \angle -64.2° |
| Approx.1 | 6.87 \angle -79.7° | 0.873 \angle -79.2° | 0.117 \angle -67.3° |
| Approx.2 | N/A | 0.225 \angle -45° | N/A |
| Measured | 6.74 \pm 1.22 \angle -79.5 \pm 8.65° | 0.915 \pm 0.0929 \angle -80.9 \pm 2.98° | 0.0934 \pm 0.0132 \angle -76.8 \pm 1.07° |

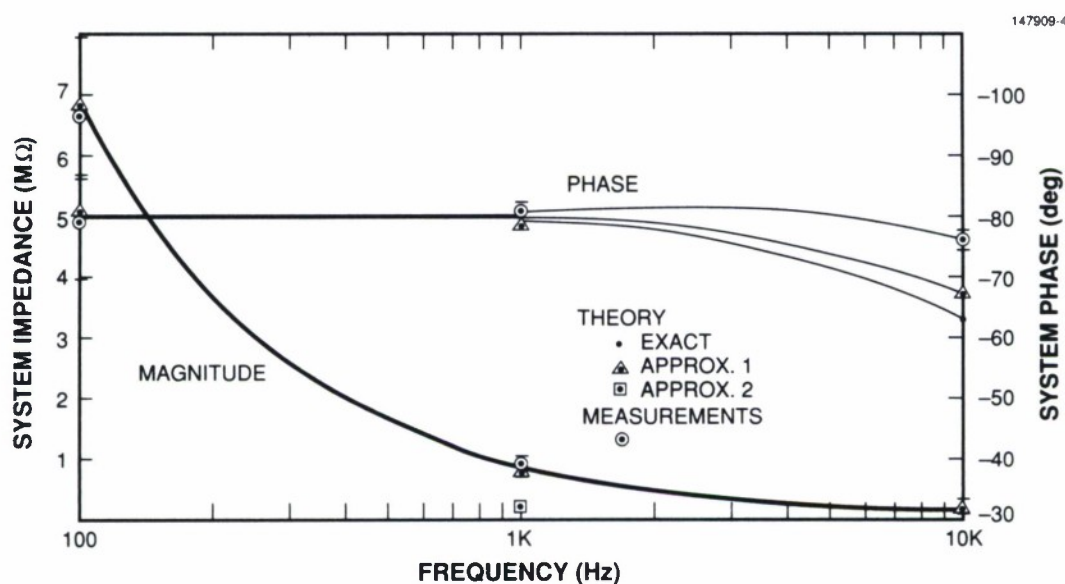


Figure 21. Theoretical and measured biochip electrode impedances.

2.4.2 Impedance Measurements of Platinized Electrodes

The measurement procedure for platinized biochips is identical to the previously outlined approach. Since the effective electrode surface area is enlarged by a factor γ following platinization, and the impedance function is inversely proportional to such surface area, the best impedance reduction through platinization is expected to be γ^{-1} .

The results of the impedance measurements taken from a biochip (with 65 operable electrodes) selected from the previously evaluated fabrication run and platinized under the conditions specified are displayed in Figure 22. The magnitude exhibits the $\omega^{-1/2}$ behavior; however, the phase varies substantially with frequency, unlike the unplatinized electrodes where the phase remains relatively constant for most of the bandwidth. Such phase variation may explain the frequency dependency of the impedance reduction, where the reduction factor γ achieved by platinization is 46 at 100 Hz, and diminishes to 8.5 at 10 kHz. Hence, the benefit of platinization is frequency dependent, with the greatest advantage experienced at lower frequencies. Another consequence of platinization is an increased deviation in the impedance values. This increase can be attributed to the nonuniform growth of the surface area among the various electrodes during platinization.

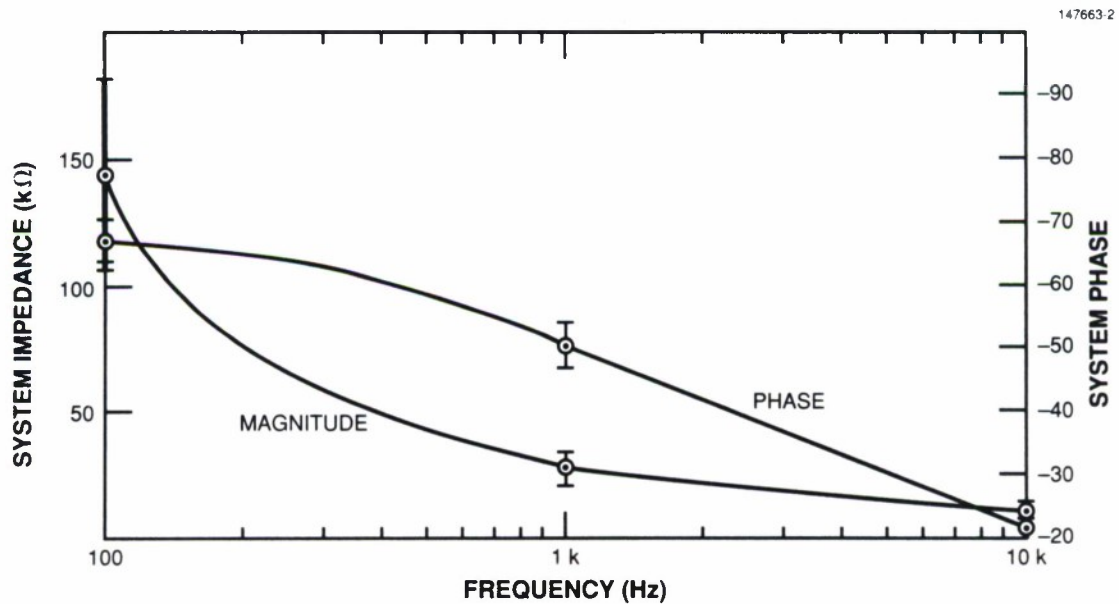


Figure 22. Theoretical and measured platinized biochip electrode impedances.

2.5 SYSTEM INTEGRATION

The integration of the neural network signal-processing system, ranging from the biochip (with microvolt analog signals) to the computer (with digital signals), is carried out in two phases as indicated in Figure 23. The initial phase provides basic technology verification, where single neural action potentials are recorded from a single biochip electrode. This phase includes both the biochip and the custom

instrumentation amplifiers to provide the higher voltage levels required by conventional data acquisition equipment and recording devices. The second phase provides an experimental neural network framework by offering near simultaneous recording and stimulation across the entire biochip electrode array (72 channels).

The following description of the system integration is top-down, beginning with the data acquisition computer and concluding with the specially designed neural chambers that house the biochip during experimentation.

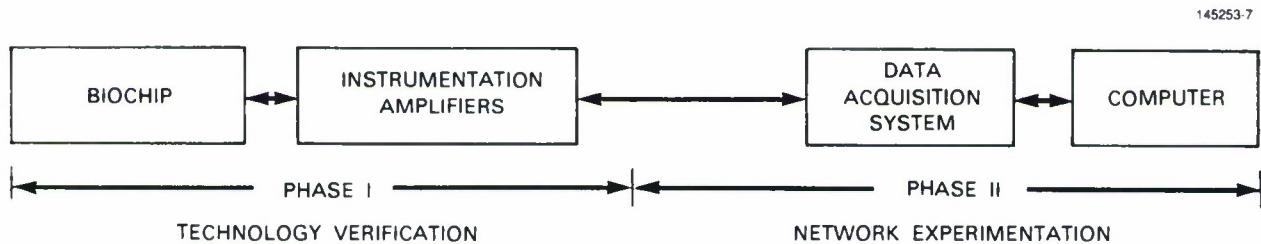


Figure 23. Neural network signal processing system.

2.5.1 Multichannel Data Acquisition

The requirements for the data acquisition system and computer are primarily driven by the number of electrodes in the biochip array and the bandwidth of the neural signals. Allowing for a generous 7-kHz neural signal bandwidth and assuming ideal Nyquist sampling, the aggregate data transfer rate required is $2 \times (7\text{-kHz/channel}) \times 72 \text{ channels} \cong 1\text{M samples/second}$. Hence, with 2 bytes/sample quantization, the A/D converter must operate at 2 Mbytes/second to enable neural signal recording across the 72-channel array. Conversely, stimulation is provided by a D/A converter with significantly less channel capacity, as only a few different stimulus patterns are needed at a given instant.

In addition to the data-transfer requirement, a high-level programming environment with real-time capability is needed to control operations during actual experimentation. For example, the electrical stimulus pattern can be altered during a given experiment, with the updated information obtained from the neural signals recorded and displayed on a graphics terminal in near real time. A multichannel data acquisition system is required to provide high-speed data acquisition, analysis, and graphical presentation.

The system selected to satisfy the requirements is illustrated in Figure 24. The Concurrent MC6700 as configured provides a main-memory data-transfer rate of 2 Mbytes/second, and a disk-transfer rate of 1.7 Mbytes/second. To achieve the high data-transfer rate, many of the acquisition operations are performed locally by the DACP module without interrupting the host CPU. This DACP module and other data acquisition modules shown in Figure 25 are inserted into the computer backplane, specifically to tailor the system to the application. The 48-channel multiplexer module expands each of the 16-channel A/D converter modules to a maximum of 64 single-ended channels.

The multiplexer input signal range is ± 10 volts, requiring substantial amplification to couple the micro-volt-level signals from the biochip to the multiplexer.

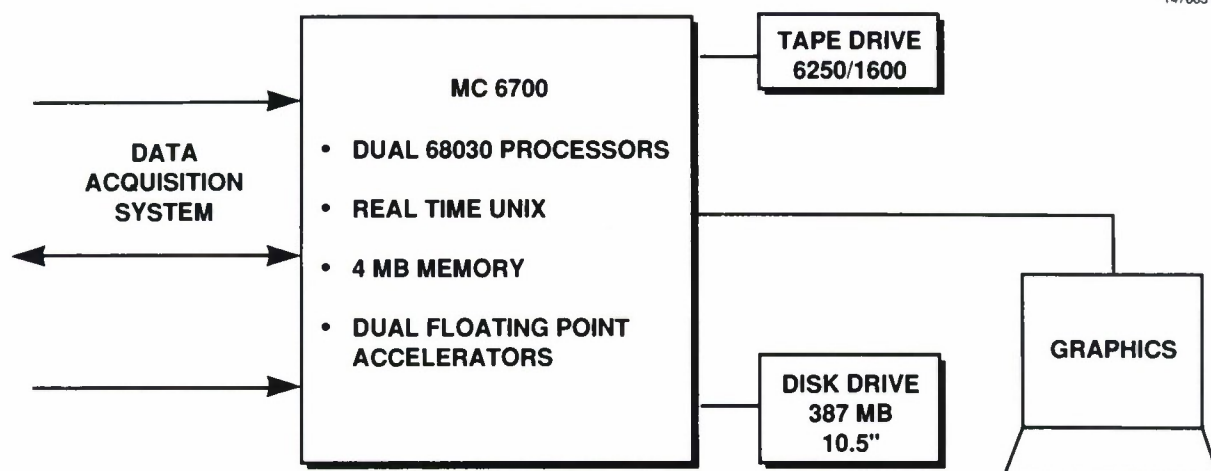


Figure 24. Data acquisition host computer system.

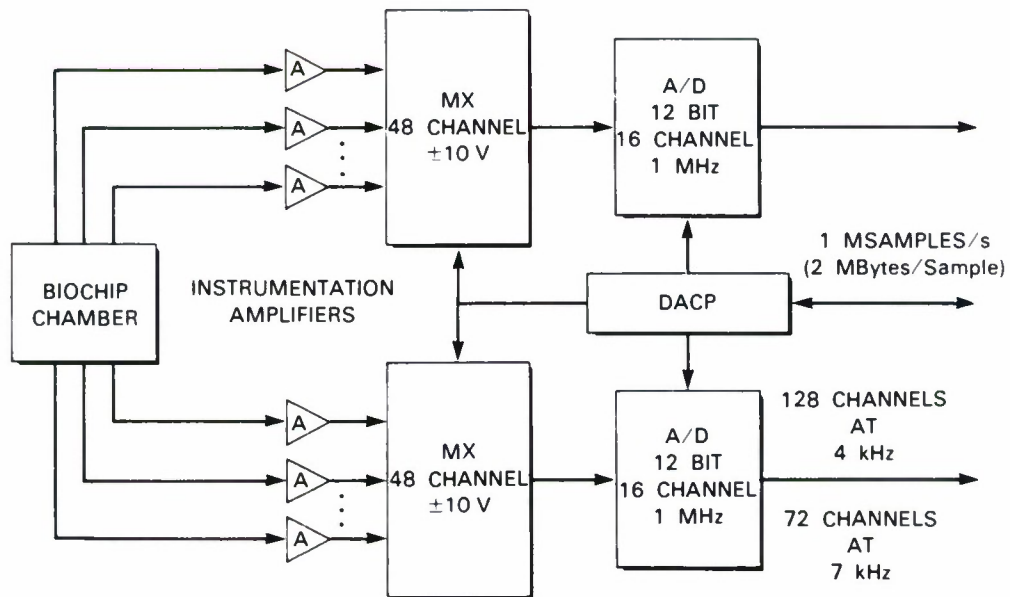


Figure 25. Data acquisition modules for interfacing with the biochip and host computer.

2.5.2 Instrumentation Amplifiers

The specifications for the 72 instrumentation amplifiers shown in Figure 25 are driven by the neural signaling properties and biological considerations. In neural signaling, the extracellular action potentials may range from 50 to 400 μV peak-to-peak, and will be found embedded in 20-40 μV thermal noise (50) if the bandwidth is generously selected to be 7 kHz. Therefore, the amplification required is approximately 50,000 \times . Because the neuron must be isolated from the electronics to avoid induced behavior artifacts, a very large input impedance is required for the amplifier. Moreover, a low-bias or offset current is required to prevent amplifier saturation when connected to the high-impedance ($\text{M}\Omega$) electrode source. As a consequence, a precision instrumentation amplifier is required with high gain, high dynamic range, low noise, and a high input impedance.

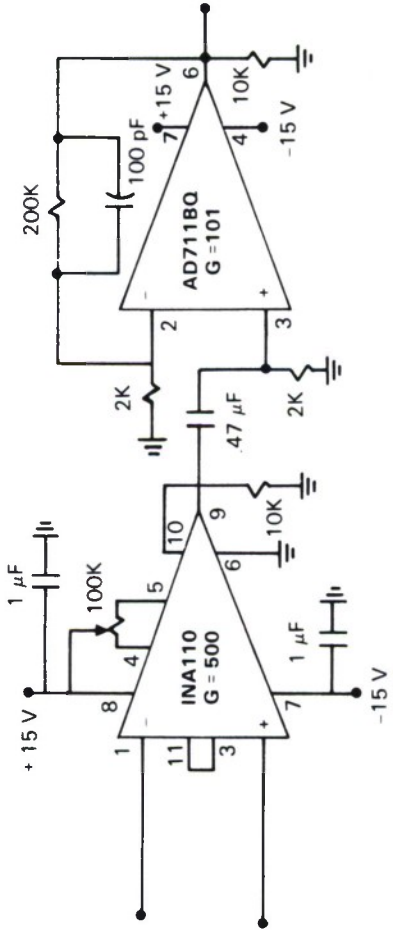
A two-stage custom amplifier satisfying these constraints was constructed from a cascade of a Burr-Brown INA110 very-high-accuracy instrumentation amplifier and a conventional operational amplifier (AD711BQ) for additional gain. The circuit is shown in Figure 26(a). The front-end amplifier offers the desired high input impedance ($1\text{T}\Omega$) by using dual precision FET buffers on the input. This design also exhibits a low DC bias current (50 pA) to avoid saturation. Finally, the variable gain for the first amplifier is set to 500 \times so that, in combination with the second stage, the overall gain is near 50,000 \times . The frequency response of the amplifier is shaped with the low-pass filtering provided by the feedback impedance of the second stage, and high-pass filtering is achieved by capacitive coupling. As displayed in Figure 26(b), the 3-dB bandpass extends from approximately 170 Hz to 8 kHz. The lower cut-off frequency is selected to filter out 60-Hz power line noise and the accompanying harmonics.

2.5.3 Neuronal Chambers

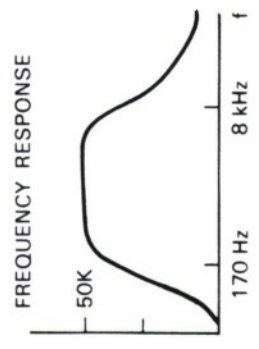
The purpose of the neuronal chamber is to provide a controlled growth environment for the neurons. Control features include both temperature and gas composition. Other desirable design features include quick biochip mechanical and electrical mounting, a sterile growth area, and optically transparent surfaces to allow transmission microscopy during experimentation.

The specific neuronal chamber employed for the mammalian cells is displayed in Figure 27. The metallic walls house a thermostatically controlled heating coil. The innermost sterilized chamber fits over the biochip package for easy assembly. The package leads extend to the four internal connectors, which are then routed to the two main exterior connectors.

The neuronal chamber designed for the invertebrate cells is shown in Figure 28. Here a standard flatpack socket with matching carrier suffices, since temperature need not be controlled. Upon packaging, the biochip is easily mounted in the carrier shown, for impedance testing and subsequent neural experimentation. The simple hinged socket cover securely mounts the biochip both mechanically and electrically. A PC board interfaces the biochip and the external connectors.



(a)



(b)

Figure 26. Schematic of (a) instrumentation amplifier and (b) corresponding frequency response.

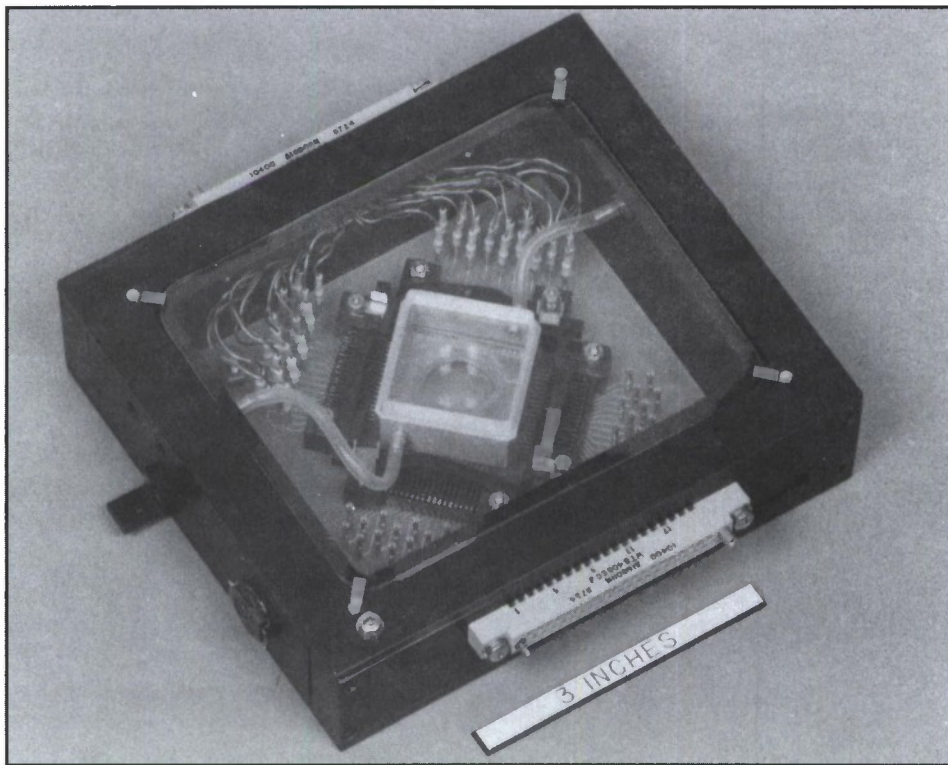


Figure 27. Warm-blooded neuronal chamber.

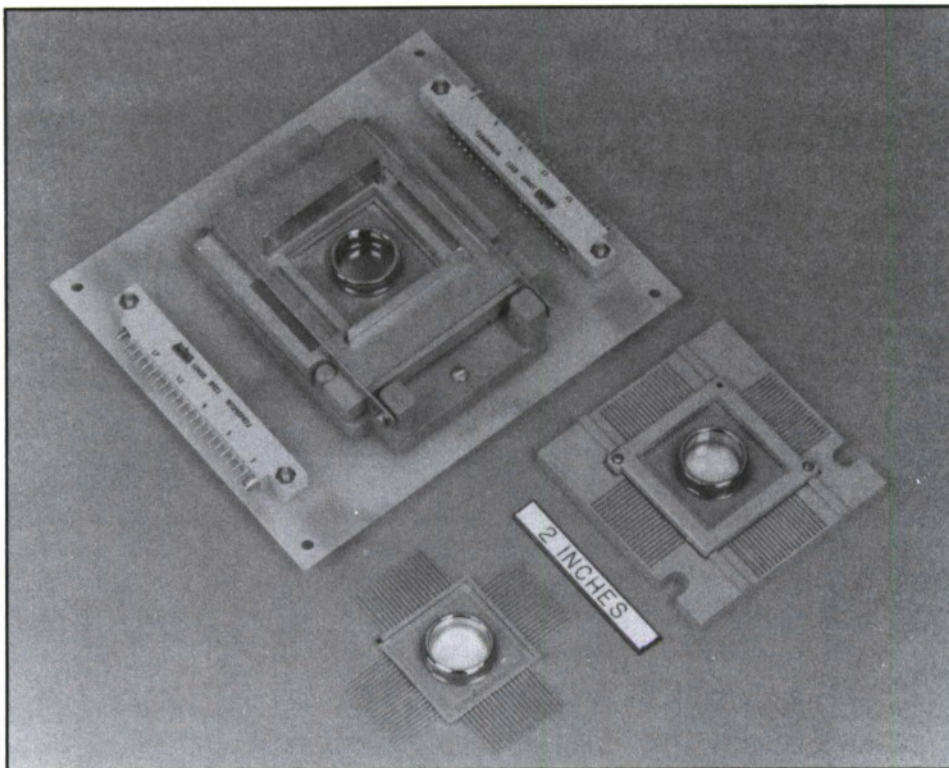


Figure 28. Cold-blooded neuronal chamber.

3. NEURAL GROWTH BIOLOGY

Electrically excitable cells from dissociated invertebrate and clonal mammalian systems are advantageous for neural network experimentation. Dissociated cell culture techniques are discussed first, followed by the clonal cell methods.

3.1 DISSOCIATED CELL CULTURES

Neurons from dissociated invertebrate systems offer particular advantages for analyzing the response properties of the biochip. One major advantage is that the cells are large (approximately 50 μm), which permits easy handling and simultaneous recording from intracellular microelectrodes and extracellular biochip electrodes. Simultaneous recording is necessary for verifying the biochip recording capability. Also, such cells require minimal life support, unlike mammalian cells which require higher temperatures and elevated CO_2 . In addition, these cells form synapses when grown in tissue culture, allowing analysis of synaptic properties. The disadvantage with dissociated invertebrate cells is the large variation in cell types within a grown network, making modeling much more complex.

To prepare neurons for the biochip, the ganglia of 2- to 10-gram-sized *Aplysia californica* sea slugs obtained from Howard Hughes Medical Facilities in Woods Hole, Massachusetts, are dissected out and washed in an incubation medium. Next, the ganglia are incubated in dispase (Boehringer Mannheim 1%, pH7.4) in an incubation medium for about 4 hours at 34°C. The base incubation medium consists of L-15 (Flow Labs) with the addition of NaCl (320mM), KCl (4.6mM), CaCl_2 (9.7mM), MgCl_2 (53.2mM), HEPES (5mM), glucose 1%, penicillin, and streptomycin. The solution is titrated to pH7.7 and sterilized by filtration. Following incubation, ganglia are washed with additional incubation medium and teased apart with fine forceps. The resulting dissociated neurons can be plated on the biochip by pipetting. The biochip culture medium consists of 0.5% methyl-cellulose in incubation medium and is kept at room temperature. Within 2 to 4 days, synaptic connections develop with morphological characteristics similar to control cultures grown in conventional glass dishes.

3.2 CLONAL CELL CULTURES

Instead of using dissociated cell cultures, in which numerous cell types occur within a single network, clonal cell cultures can be employed. This approach allows the network to be tailored for specific experiments and applications. Identical cells can be networked on the biochip to provide a system amenable to mathematical analysis. Since the cell line is immortal, an infinite supply of cells can be obtained inexpensively. Although these tailored clonal neural circuits may well exhibit basic network properties, they are not expected to represent *in vivo* neural systems.

To produce the clonal cells, precursor cells are first extracted from a fetal rat cerebellum. As illustrated in Figure 29, a temperature-sensitive oncogene is expressed into the precursor cell through a virus. The oncogene, now within the precursor cell, represents the control mechanism that causes the precursor cell to divide or differentiate. At the lower temperature, the cell divides; at the elevated temperature, the cell differentiates into one of several types.

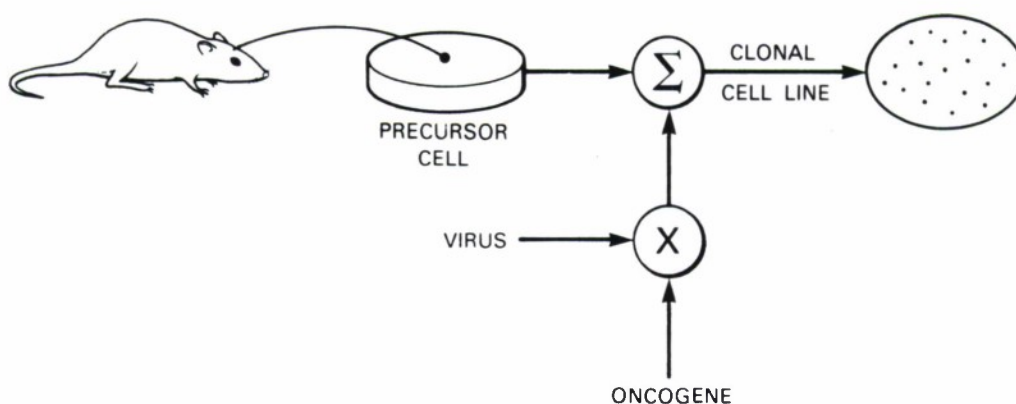


Figure 29. Clonal cell generation.

Specifically, the ST15A cell line used can differentiate into cells with either neuronal or astrocytic properties depending on the serum conditions [21]. These ST15A cells have been shown to differentiate uniformly into muscle cells, which are advantageous for microelectrode penetration due to the network growth in uniform, fused, synclinal sheets.

The ST15A culture procedure begins by trypsinizing cells grown in 10% fetal calf serum (FCS) in DMEM at 33°C. These cells are plated in the biochip culture well containing the same fluid. One day after the cells became confluent, the medium is changed to 10% horse serum (HS) in DMEM and the temperature is changed to 39°C. Five days later, multinucleate cells are formed and ready for experimentation. The culture remains operable for at least one week without a change of medium. When the medium is changed, the fresh medium is prewarmed in the culture incubator with the container lid loosely capped to balance the medium's pH. Only one third of the medium volume in the biochip culture well is replaced at a time.

An alternative cell line, C2, proved easier to differentiate and grow on the biochip. Since the differentiated C2 muscle cells are rather long, intracellular stimulation is also easier. The C2 cell culture preparation is the same as ST15A cells, except that one day after the culture becomes confluent, the medium is changed to 5% calf serum (CS) in DMEM and the temperature held constant.

4. NEURAL MEASUREMENTS

This section describes the capabilities offered through the integration of electrical engineering and biology. Using the technology described in the preceding sections, noninvasive neural recording and stimulation are achieved with the biochip.

4.1 NEURON RECORDING

The following two measurement experiments demonstrate the ability to record from single neurons and a network of neurons grown and synaptically coupled on the biochip.

4.1.1 Single Neuron

The objective of the single neuron recording experiment is to verify the basic technology development and recording operation of the biochip. A conventional glass-coated intracellular microelectrode is the benchmark recording device. The 30-M Ω microelectrode is made of glass tubing with 1.0-mm outside and 0.58-mm inside diameters, filled with 3M K-acetate.

The procedure begins by growing dissociated *Aplysia* neurons on the biochip surface. At maturation, an intracellular probe is inserted into a candidate neuron residing over an electrode as shown in Figure 30. The neuron is subsequently stimulated by the intracellular probe with a current pulse which depolarizes the neuron. Recorded neuron signals from the intracellular probe (superposition of input stimulus and neuron output) and the extracellular biochip electrode are also shown in Figure 30. The signals are displayed and recorded with a Nicolet 4049 digital oscilloscope in conjunction with a Nicolet XF-44 disc recorder. Both the intracellular and extracellular recordings display three action potentials with good correlation. The price for noninvasive recording is lower SNR; however, the SNR is sufficient for the microvolt-level extracellular neural response to be easily observed.

4.1.2 Synaptically Coupled Neurons

The second recording experiment demonstrates that a network of neurons can be grown on the biochip. Specifically, the network was proven synaptically coupled by displaying highly correlated neural signals recorded from two connecting neurons. Both spontaneously active and artificially stimulated networks are employed.

The experiment begins by growing *Aplysia* neurons on the biochip. Within days, the neural processes grow to make connections with neighboring neurons. In approximately 3 days, the network will be mature and display abundant convoluted connections, as shown by the electron micrograph in Figure 31. Although most of the neural processes channel along the surface of the biochip, occasionally some can be found suspended between neurons.

Conventional intracellular probes are then inserted into two neurons which appear visually connected. For the artificially stimulated network, one neuron (designated the presynaptic neuron) is stimulated with a positive pulse current, while signal records are taken of both the presynaptic and connecting postsynaptic neurons. Notice from Figure 32 that the signals display definite correlation, substantiating

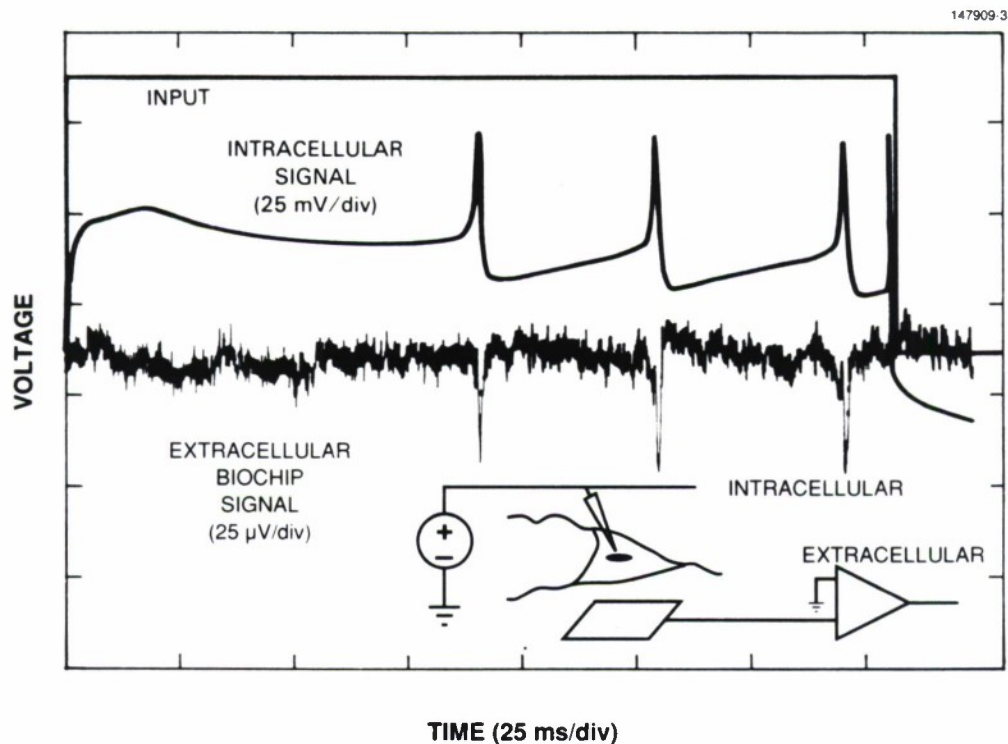


Figure 30. Single-neuron recording from conventional and biochip electrodes.

the formation of a chemical synapse. Specifically, the induced presynaptic neural action potentials are seen to promote postsynaptic neural action potentials in two of the three instances. On one occasion, the postsynaptic neuron responds with only a slight graded response, insufficient to warrant an action potential.

Results from the spontaneously active network are shown in Figure 33. Here no external stimulus is applied; rather, an active rhythmic neuron is selected as the presynaptic neuron, while a connecting neuron is intracellularly probed to obtain the accompanying postsynaptic neural response. The postsynaptic neuron responds to each presynaptic neural input with a correlated graded potential. Sometimes the graded potential is strong enough to elicit an action potential as displayed. Again, strong correlation in presynaptic and postsynaptic neural signals confirm synaptic connection.

4.2 NEURON STIMULATION

Additional experiments demonstrated the ability to elicit neural action potentials electrically, using the electrodes residing on the biochip.

To demonstrate on-chip stimulation capability with the unipolar electrodes, *Aplysia* neurons are grown on the biochip surface and allowed to mature. Next, a candidate neuron residing over an electrode on the biochip is selected for stimulation. A conventional intracellular electrode is then inserted for recording purposes, specifically to verify that the on-chip stimulus signal promotes an action potential. The biochip unipolar extracellular electrode is subsequently driven by a symmetric voltage signal source as displayed in Figure 34. The stimulation pulse generator consists of a WP Instruments interval generator 1830, pulse train module 1631, and stimulus isolator 1850A. Also shown in the figure is the resulting intracellular recording illustrating the successful depolarization of the neuron leading to the action potential. Notice that the time between the stimulus ending and the beginning of the action potential response is almost 125 ms. This time represents the maximum time for switching an electrode from stimulation (volt-level output) to recording (microvolt-level input) mode. Therefore, a single biochip electrode can be employed for both global stimulation and subsequent local recording.

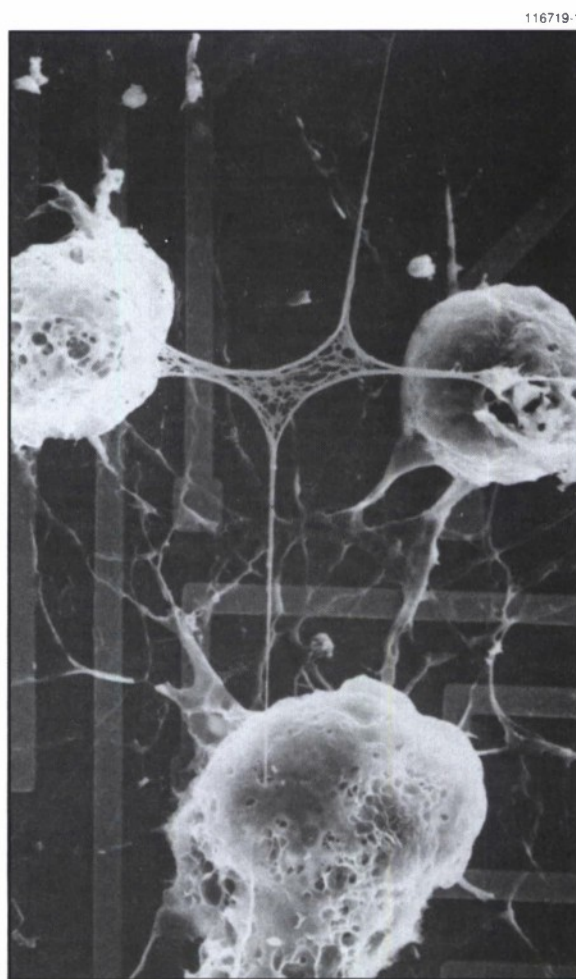


Figure 31. Electron micrograph of synaptically connected neurons on biochip surface.

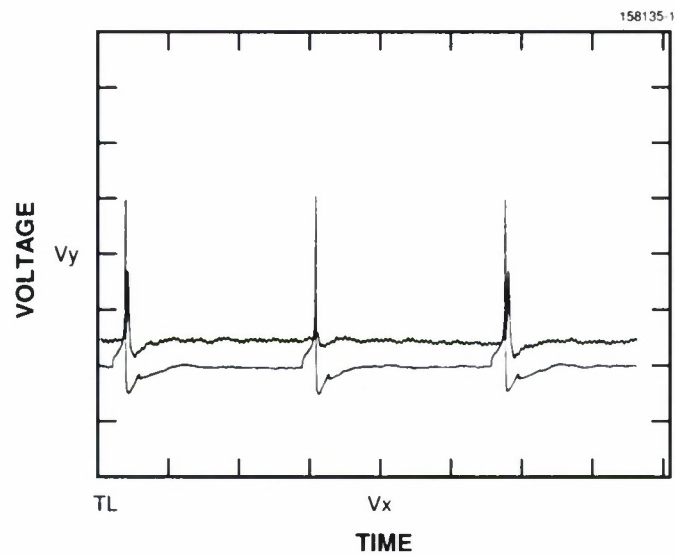


Figure 32. Recorded signals from artificially stimulated, synaptically coupled neurons on biochip surface.

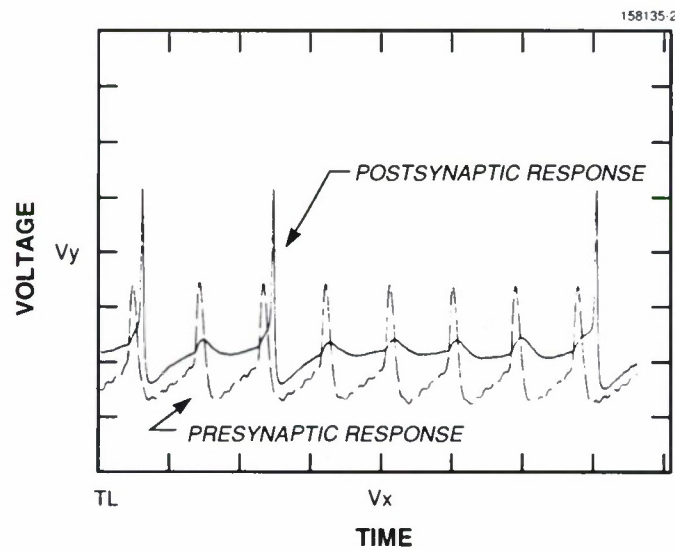


Figure 33. Recorded signals from spontaneously active, synaptically coupled neurons on biochip surface.

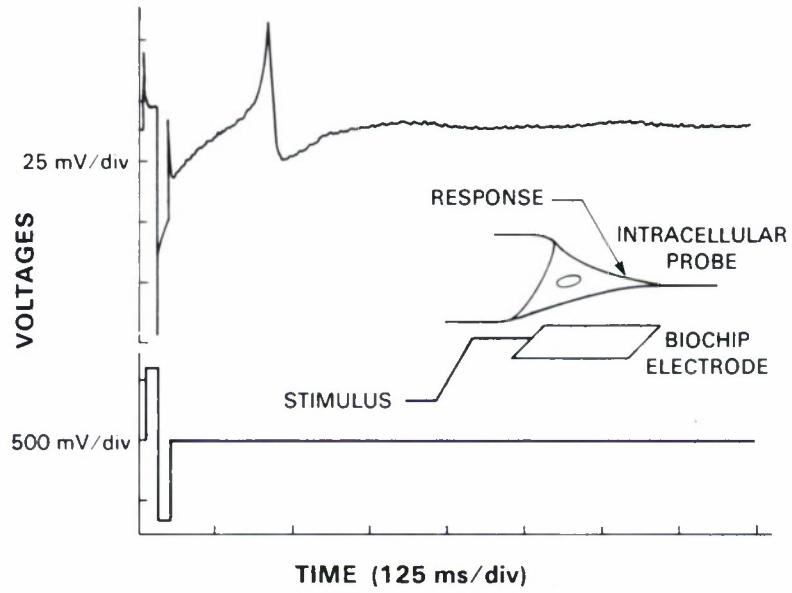


Figure 34. On-chip neuron stimulation results using unipolar biochip electrode.

5. CONCLUSION

In conclusion, the biochip technology presented provides effective interface between living cells and electronics. Specifically, long-term noninvasive multisite recording and stimulation capability is achieved. Such an interface built upon a continuing multidisciplinary collaborative effort (electrical engineering, biology, physics) can be instrumental in both future information technology and medicine. Biologically inspired computer architectures that exploit the principles of superior biological information processing may become reality. In addition, the interface also supports experimentation with medical prosthetic devices for restoration of nerve function. In all, such technology represents a significant new scientific tool.

6. REFERENCES

1. J.J. Hopfield, "Neural networks and physical systems with emergent collective computational abilities," *Proc. Natl. Acad. Sci., USA* 79, 2554-2558 (1982).
2. S. Grossberg, *The Adaptive Brain*, Amsterdam: North Holland (1986), vols. I and II.
3. T. Kohonen, *Self Organization and Associative Memory*, Berlin: Springer Verlag (1984).
4. D.E. Rumelhart, G.E. Hinton, and R.I. Williams, "Learning internal representations by error propagation," in D.E. Rumelhart, J.L. McClelland (eds.), *Parallel Distributed Processing*, Cambridge: MIT Press (1986), vol 1.
5. T. Sejnowski and C.R. Rosenberg, "NETalk: A Parallel Network that Learns to Read Aloud," John Hopkins University, Baltimore, Md., Tech Report JHU/EECS-86-01 (1986).
6. R. Linsker, "From basic network principles to neural architecture: emergence of orientation columns," *Proc. Natl. Acad. Sci., USA* 83, 8779-8783 (1986).
7. R. Lippmann and B. Gold, "Neural-net classifiers useful for speech recognition," IEEE 1st International Conference on Neural Networks, San Diego, CA, 21-24 June (1987).
8. W. Huang and R. Lippmann, "Comparisons between neural net and conventional classifiers," IEEE 1st International Conference on Neural Networks, San Diego, CA, 21-24 June (1987).
9. R. Levine, "Neural Network Performance on the Stochastic Exclusive-Or Problem," MIT Lincoln Laboratory, Lexington, Ma., Technical Rep. 808 (8 July 1985), DTIC ADA197789.
10. Y.S. Abu-Mostafa and D. Psaltis, "Optical neural computers," *Scientific American*, 88-95 (1987).
11. E. Kandel, "Small systems of neurons," *The Brain, A Scientific American Book*, San Francisco: W. H. Freeman and Company (1979).
12. C. Thomas, P. Springer, G. Loeb, Y. Berwald-Netter, and L. Okum, "A miniature microelectrode array to monitor the bioelectric activity of cultured cells," *Experimental Cell Research* 74, 61-66 (1972).
13. G. Gross, "Simultaneous single unit recording in vitro with a photoetched laser deinsulated gold multi microelectrode surface," *IEEE Trans. on Biomedical Engineering* BME-26, no 5, 273-279 (1979).
14. M. Droge, G. Gross, M. Hightower, and L. Czinsky, "Multielectrode analysis of coordinated, multisite, rhythmic bursting in cultured CNS monolayer networks," *The Journal of Neuroscience* 6, 1583-1592 (1986).
15. J. Pine, "Recording action potentials from cultured neurons with extracellular microcircuit electrodes," *Journal of Neuroscience Methods* 2, 19-31 (1980).
16. D.A. Robinson, "The electrical properties of metal electrodes," *Proceedings of the IEEE* 56, No. 6 (1968).

17. P.W. Davies, "The oxygen cathode," in W.L. Nastak (ed.), *Physical Techniques in Biological Research*, New York: Academic Press (1962), vol. 4, Chap. 3.
18. R. Gesteland, B. Howland, J. Lettvin, and W. Pitts, "Comments on microelectrodes," *Proc. IRE* 47, 1856-1862.
19. H. Schwan, "Determination of biological impedances," in W.L. Nastak (ed.), *Physical Techniques in Biological Research*, New York: Academic Press (1962), vol. 6, Ch. 6.
20. H. Baldwin, S. Frank, and J.Y. Lettvin, "Glass-coated tungsten microelectrodes," *Science* 148, 1462-1463 (1965).
21. K. Frederiksen, J. Jat, N. Valtz, D. Levy, and R. McKay, "Immortalization of precursor cells from the mammalian CNS," *Neuron* 1, 439-448 (1988).

